Computers and Fluids 268 (2024) 106109

Contents lists available at ScienceDirect

Computers and Fluids

journal homepage: www.elsevier.com/locate/compfluid

A compressible multiphase Mass-of-Fluid model for the simulation of laser-based manufacturing processes

Constantin Zenz [a,*], Michele Buttazzoni [a], Tobias Florian [a], Katherine Elizabeth Crespo Armijos [a], Rodrigo Gómez Vázquez [a,b], Gerhard Liedl [a], Andreas Otto [a]

[a] Institute of Production Engineering and Photonic Technologies, TU Wien, Getreidemarkt 9, 1060, Vienna, Austria
[b] LKR Light Metals Technologies, Austrian Institute of Technology, Giefinggasse 2, 1210, Vienna, Austria

ARTICLE INFO

Keywords:
Laser material processing
Multiphase flow
Compressibility
OpenFOAM
Volume-of-Fluid
Mass-of-Fluid

ABSTRACT

A new model for compressible multiphase flows involving sharp interfaces and phase change is presented, that uses a variant of the Volume-of-Fluid model to track phases by advecting their respective mass, and is hence called Mass-of-Fluid model. The framework is aimed at predicting the coupled multi-physical phenomena involved in most processes encountered in laser material processing, with the aim of minimizing a priori assumptions on the nature of the process. Emphasis is put on the multiphase fluid flow model, especially on the treatment of compressibility and phase change. The model's accuracy and suitability is demonstrated on problems of increasing complexity, including well-known benchmarks and problems encountered in laser material processing, where simulation results are compared to experimental observations.

1. Introduction

High power lasers are widely used within various industries for a broad variety of manufacturing processes due to their versatility. Some examples of the many applications include welding, cutting, powder bed fusion, drilling and cladding [1,2]. Accurate, physics-based models for laser-material interaction, and the resulting physical phenomena are needed to understand, design and optimize these processes [3]. Due to the multi-physical nature of the process, mechanistic modeling poses a complex challenge. In Fig. 1, an illustrative example of a laser material processing simulation conducted with the here-presented model is given, highlighting some of the involved phenomena and the complexity of the process. Another example for a process is shown in Fig. 2, where nanosecond long laser pulses are used for the ablation of copper, where the molten copper is entrained by shock waves that form in the ambient gas. Although both processes are very different in terms of time- and length scales and the dominant physical processes at play, they follow the same underlying physical principles and can both be efficiently simulated using the same model.

Laser-material processing models are typically dedicated to one process, where historically the focus has been mainly on laser welding, and more recently also on additive manufacturing processes, such as laser powder bed fusion or direct energy deposition. Those process-specific models typically employ assumptions which are justified in the context of the respective process or investigation but limit their validity to a narrow set of applications. An example is the laser cutting model of Zhao and Cheng [4], where evaporation and the thus induced recoil pressure are neglected, limiting its applicability, according to the authors, to cutting of sufficiently thin sheets. Regarding more general approaches, Cho and Na [5] modeled keyhole welding with a pulsed laser source taking into account Fresnel absorption and multiple reflections within the keyhole, not taking into account any vapor phases and employing an explicit recoil pressure only depending on local temperature and constant far field pressure and evaporation efficiency. Courtois et al. [6] modeled beam propagation through the Maxwell equations and included the gas phase in their model, but did not distinct between ambient gas and metal vapor, assuming incompressible gas phases. They furthermore neglected the temperature dependency of surface tension, and hence Marangoni convection. Tan and Shin [7] incorporated a compressible description of the gas phases and included their flow description in the model, but explicitly calculated the recoil pressure, applying it in the form of a boundary condition at the interface between gaseous and condensed matter, assuming a constant evaporation efficiency. Ai et al. [8,9] included the gas phase in their model, assuming incompressibility and not differentiating between ambient gas and metal vapor, modeling the effect of recoil pressure explicitly and

* Corresponding author.
E-mail addresses: constantin.zenz@tuwien.ac.at (C. Zenz), michele.buttazzoni@tuwien.ac.at (M. Buttazzoni), tobias.florian@tuwien.ac.at (T. Florian), katherine.crespo@tuwien.ac.at (K.E. Crespo Armijos), rodrigo.gomez@ait.ac.at (R. Gómez Vázquez), gerhard.liedl@tuwien.ac.at (G. Liedl), andreas.otto@tuwien.ac.at (A. Otto).

https://doi.org/10.1016/j.compfluid.2023.106109
Received 7 June 2023; Received in revised form 28 September 2023; Accepted 8 November 2023
Available online 10 November 2023
0045-7930/© 2023 The Author(s). Published by Elsevier Ltd. This is an open access article under the CC BY license (http://creativecommons.org/licenses/by/4.0/).

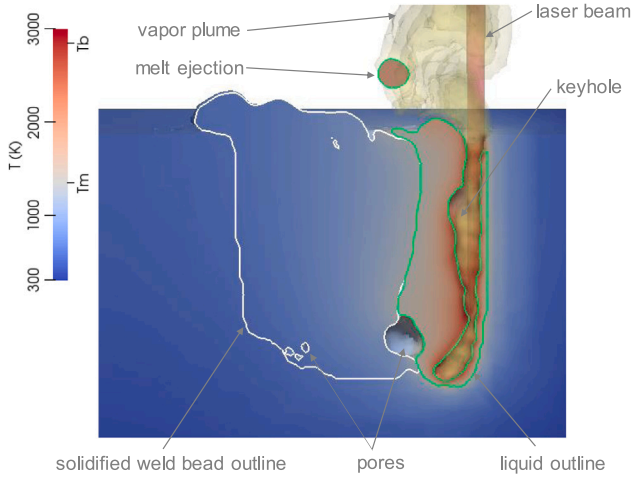

Fig. 1. Three-dimensional simulation (longitudinal section) of copper processing through laser beam welding (result from simulation presented in Section 4.5).

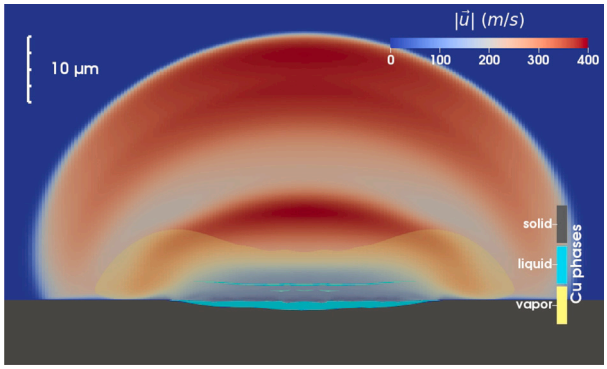

Fig. 2. Two-dimensional simulation of copper processing through laser ablation using nanosecond pulses. Shock waves form due to the rapid expansion of heated gas, entraining liquid copper.

only depending on the local temperature of the liquid. Similarly, Yu and Zhao [10] also assume incompressibility and incorporate the gas phase in their model and explicitly handle forces between gaseous and condensed matter. One widely used tool for the simulation of various laser-based material processing scenarios is the commercial software *Flow-3D*, where incompressibility is assumed and gaseous phases are neglected and their effect on condensed matter (e.g., in the form of recoil pressure) is modeled explicitly through boundary conditions [11–13]. Some studies report the use of frameworks very similar to that of *Flow-3D* but do not provide information on which software framework (or in-house code) was used to implement the model. One such example is the model of Feng et al. [14] used to simulate partial and full penetration keyhole welding. Flint et al. [15,16] presented a model including component-wise phase changes of different elements of, e.g., an alloy. Although employing an incompressibility assumption for all phases, they modified the continuity equation through a volume dilation term accounting locally for the compression and expansion during evaporation and condensation, where thus the recoil pressure is an implicit result of the volume dilation. The rate of evaporation and condensation is a function of temperature only (without taking into account local pressure). Yu and Zhao [10] also included gas phases and their flow description in their model, again assuming incompressibility and incorporating an explicitly calculated recoil pressure, focusing on accurate spatial resolution of evaporation phenomena.

The studies mentioned here represent only a brief and non-comprehensive overview of some more recent multiphysical models and their main fluid-mechanical assumptions. For a wider overview on the state of the art and typical model assumptions employed in modeling of laser-material processing, we refer the reader to the review of Dal and Fabbro [17] focused on the process of laser beam welding, and the review of Cook and Murphy [18] focused on selective laser melting (i.e., powder bed fusion).

It was recently shown by Shu et al. [19] that even for low power additive manufacturing scenarios, where no keyhole is present (conduction-mode laser melting), accurate modeling of convective heat transport, and therefore melt flow, is needed to correctly predict the thermal history and three-dimensional weld bead shape of a part (even if results of a non-convective model are validated by comparing against experimental weld bead cross sections). This once more highlights the need for multi-physical modeling, even in fairly simple scenarios of laser material processing. A truly universal model for laser material processing should, like the corresponding real-world process, only need process and material parameters, and initial and boundary conditions as inputs and be able to then predict the process. This necessity of a universal model requires the number of process-specific assumptions to be minimized. We therefore omit typical assumptions [17] such as the incompressibility of fluid phases or the exclusion of vapor phases. Over the course of developing a universal multi-physical model for laser-based manufacturing, covering both micro- and macroscopic processes using continuous wave [20–27] and pulsed lasers [28–30], a novel approach to model compressible segregated multiphase flows undergoing phase changes was derived. The model, which we call Mass-of-Fluid model, is presented in Section 2. Details on the numerical implementation are provided in Section 3. Then, simulation results from a series of test cases of increasing complexity are presented, with the aim of validating the model and its implementation and demonstrating its universality.

2. Model description and governing equations

We employ a homogeneous equilibrium mixture model for the fluid-mechanical multiphase problem, where the Navier–Stokes equations and energy equation are solved for a mixture of N phases, locally assuming average thermophysical properties and a shared velocity, pressure and temperature. In this context, each phase i corresponds to one aggregation state of one material. Therefore, in a typical application within laser material processing of a single material (e.g., *metal*), we encounter the phases *solid metal*, *liquid metal*, *metal vapor* (or multiple instances of these, in the case of multi-material simulations) and *ambient gas*. Additionally, we denote the phase *resolidified material*, i.e., solid material which solidified from melt, as this proves convenient for post-processing simulation results, e.g., visualizing the weld bead depth. Furthermore, this gives the opportunity of employing different material properties for the green state material and the processed (molten and solidified) material.

2.1. Momentum equations

The continuity and momentum equations for the mixture of phases read

$$\frac{\partial \rho}{\partial t} + \nabla \cdot (\rho \boldsymbol{u}) = 0, \tag{1}$$

and

$$\frac{\partial (\rho \boldsymbol{u})}{\partial t} + \nabla \cdot (\rho \boldsymbol{u}\boldsymbol{u}) = -\nabla p + \nabla \cdot \boldsymbol{\tau} - \boldsymbol{S}_B + \boldsymbol{S}_S + \boldsymbol{S}_D, \tag{2}$$

where $\boldsymbol{u}$, p, ρ, and $\boldsymbol{\tau}$ denote velocity, pressure, density, and viscous stress tensor of the mixture, respectively. Furthermore, $\boldsymbol{S}_B$, $\boldsymbol{S}_S$, and $\boldsymbol{S}_D$ denote sources of momentum due to gravity, surface tension, and a source term for movement restriction in the mushy zone (a mixture of solid and liquid material during solidification of an alloy) and solid regions, respectively. The source $\boldsymbol{S}_D$ is modeled as a porous bed

through Darcy's law [31] following the Carman–Kozeny equation as [32]

$$\boldsymbol{S}_D = -\frac{\mu}{A_{perm}} \frac{\left(\alpha_{solid}\right)^2}{\left(1-\alpha_{solid}\right)^3 + \delta} \boldsymbol{u}, \tag{3}$$

where α_{solid}, and μ denote the volume fraction of solid material, and the viscosity of the mixture, respectively. A_{perm} is the permeability area of the porous bed which is employed to model the mushy zone, usually set to $A_{perm} \approx 10^{-12}$ m^2, and $\delta = 10^{-6}$ is a small constant to prevent a division by zero.

Surface energies at phase-pair interfaces are calculated from individual phases' surface energies σ_i, assuming non-polar solid surfaces, as [33]

$$\sigma_{i,j} = \sigma_i + \sigma_j - 2\sqrt{\sigma_i \sigma_j}, \tag{4}$$

with $\sigma_i = f(T)$ typically being temperature-dependent, from which we calculate a continuum surface tension force [34] as

$$\boldsymbol{S}_S = \sum_{i,j \forall i<j} \nabla \cdot \left[\sigma_{i,j} \left(\alpha_j \nabla \alpha_i - \alpha_i \nabla \alpha_j\right)\right], \tag{5}$$

where α_i denotes the volume fraction of phase i, thus $\boldsymbol{S}_S$ only takes values within interface regions of finite thickness. However simple the surface tension force model of Eqs. (4)–(5) is, it bears the advantage of only requiring individual phases' surface energy values (i.e., the phase-vacuum interface values of surface tension) as input parameters, without having to specify contact angles or interface properties.

Body forces include only the gravitational force and are modeled as

$$\boldsymbol{S}_B = \boldsymbol{g} \cdot (\boldsymbol{h} - \boldsymbol{h}_{ref}) \nabla \rho, \tag{6}$$

where $(\boldsymbol{h} - \boldsymbol{h}_{ref})$ denotes the position in space with respect to an arbitrary reference point $\boldsymbol{h}_{ref}$ and $\boldsymbol{g}$ is the gravity vector. Forces due to evaporation-induced recoil pressure are not explicitly modeled as they are an implicit result of the compressible multiphase model (phase change issues a change in volume due to the difference in phases' densities, resulting in a change in pressure). The same holds for forces due to thermally induced expansion and contraction. The here-presented model is, to the authors' best knowledge, the only published fluid-dynamical model of laser material processing to date that is not relying on an explicitly calculated evaporation-induced recoil pressure, except for the model of Flint et al. [15], where the incompressible continuity equation is modified through a source term active at phase interfaces during evaporation to account for the associated volumetric change and thus recoil pressure.

2.2. Mass-of-Fluid method

One of the most predominant models for the simulation of segregated phases using the Finite Volume Method (FVM) is the Volume-of-Fluid (VoF) method, developed by Hirt and Nichols [35]. Within that framework, phase volume fractions are tracked via advection on a previously obtained velocity field. The thus obtained phase volume fraction distribution is used to update the spatial distribution of material properties such as the density. As this approach is not inherently mass conservative for compressible phases, we propose an altered scheme which we call *Mass-of-Fluid* (MoF) method. Here, we directly track the conserved quantity of the phases' mass, which leads to mass conservative advection and phase changes even in highly compressible scenarios. The implementation of phase changes between phase-pairs is relatively straightforward within this framework.

We define a quantity ρ_i for each phase i of an N-phase problem as

$$\rho_i = \frac{m_{i,CV}}{V_{CV}}, \tag{7}$$

where $m_{i,CV}$ is the mass of phase i within a control volume V_{CV}. Note that CV denotes the hypothetical concept of a control volume, and ρ_i is a function continuous in space and time governed by Eq. (9). The mixture density ρ (i.e., average density of the mixture of N phases) is obtained through summation as

$$\rho = \sum_{i=1}^{N} \rho_i. \tag{8}$$

We introduce a conservation equation for each phase's local mass density reading

$$\frac{\partial \rho_i}{\partial t} + \nabla \cdot \left(\boldsymbol{u} \rho_i\right) = \dot{\rho}_{i,m} + \dot{\rho}_{i,s} + \dot{\rho}_{i,e} + \dot{\rho}_{i,c}, \tag{9}$$

where the four source terms on the RHS of Eq. (9) represent the change in ρ_i due to melting, solidification, evaporation and condensation, respectively. Eq. (9) represents phase-wise continuity equations that always fulfill Eq. (1), i.e., global continuity, due to Eq. (8) and the fact that for any phase pair i, j undergoing phase change, the source terms on the RHS of Eq. (9) sum to zero. For example, for i, j denoting a solid and liquid phase that exchange mass through melting, $\dot{\rho}_{i,m} = -\dot{\rho}_{j,m}$. Hence,

$$\sum_i^N \dot{\rho}_{i,m} = 0, \tag{10}$$

$$\sum_i^N \dot{\rho}_{i,s} = 0, \tag{11}$$

$$\sum_i^N \dot{\rho}_{i,e} = 0, \tag{12}$$

$$\sum_i^N \dot{\rho}_{i,c} = 0. \tag{13}$$

The four source terms on the RHS of Eq. (9) representing phase changes are defined in Section 2.4. Eq. (9) provides a full description of the temporal and spatial distribution of phases within the mixture.

While the mixture density is obtained from Eq. (8), other properties of the mixture (e.g., thermophysical properties) are obtained through volume-weighted averaging based on the individual phase volume fractions, α_i. Generally, we choose different physically motivated averaging approaches for different physical quantities (e.g., harmonic averaging is often reasonable in the case of thermal conductivity), but for the sake of simplicity we only use arithmetic averaging throughout this work s.t. for any mixture physical property ϕ,

$$\phi = \sum_i^N \alpha_i \phi_i, \tag{14}$$

where ϕ_i denotes the physical property value of the respective phase i and α_i is the volume fraction of phase i. The relationship between density and pressure of all phases is modeled via the Tait equation [36,37] as

$$\rho_{th,i}(p) = \rho_{ref,i} \sqrt[\gamma_i]{\frac{p + B_i}{p_{ref} + B_i}}. \tag{15}$$

Here, $\rho_{th,i}$ denotes the density of phase i, i.e., a temperature- and pressure-dependent material property of phase i, not to be confused with ρ_i. Furthermore, $\rho_{ref,i} = \rho_{th,i}(p_{ref})$ is the temperature-dependent density of phase i at reference pressure p_{ref}, which is the temperature-dependent density value reported in the respective Tables of Section 4 and Appendix as simulation input parameter, with $p_{ref} = 10^5$ Pa. B_i and γ_i are empirical constants (Tait pressure and heat capacity of a liquid, respectively), where we use the bulk modulus K_i to define $B_i = K_i/\gamma_i$. The parameter γ_i influences the compressibility behavior of the phase, where $\gamma_i = 1$ yields the case of an ideal gas, and $\gamma_i = 7.15$ is a typical value for water. Gaseous behavior that diverges from that of an ideal gas can conveniently be accounted for by choosing an appropriate value for γ. Regarding condensed phases, it is difficult to obtain a value for γ for fluids other than water, but the difference only becomes relevant for extreme pressure changes. Therefore, for most scenarios, if no other data is available, we choose $\gamma_{cond} = 7.15$ for all condensed (solid and liquid) phases. Especially for solid phases, the value of γ is not too relevant in most cases, as the absolute value of K (and thus B) is of several orders of magnitude higher than that of a liquid. Fig. 3

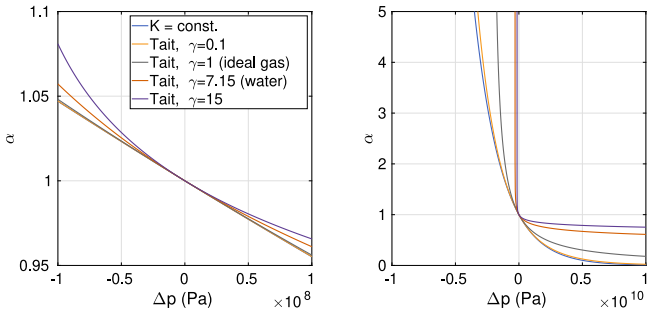

Fig. 3. Comparison of α with respect to Δp for liquid water, using different assumptions of bulk modulus-pressure dependence, dK/dp. Left and right plot are identical, except for the value range of Δp.

shows the relationship between a pressure change and the resulting change in volume (represented by the volume fraction) as determined by Eq. (15) for different values of γ and for the assumption of a constant compressibility (and hence bulk modulus).

The volume fraction α_i needed for evaluation of Eq. (14) is implicitly defined through ρ_i and $\rho_{th,i}$.

2.3. Energy equation

Due to the homogeneous equilibrium mixture assumption, all phases share a common temperature T, with the gradient of T being relevant for heat conduction. Convective transport however, is associated with the individual phases and their motion. We thus decouple convective and conductive transport of energy in the following manner. Convective transport of energy is ensured through N equations of the form

$$\frac{\partial H_i}{\partial t} + \nabla \cdot \left(\boldsymbol{u} H_i\right) + S_{p,i} = Q_{abs,i} + \dot{H}_{i,m} + \dot{H}_{i,s} + \dot{H}_{i,e} + \dot{H}_{i,c}, \tag{16}$$

where $H_i = \rho_i h_i$ denotes the energy of phase i, with h_i denoting the specific energy of phase i. The last four source terms on the RHS of Eq. (16) represent the change in energy of phase i due to phase change, analogously to Eq. (9). The energy of the mixture is obtained through summation, i.e.,

$$H = \sum_{i=1}^{N} H_i. \tag{17}$$

The source term $Q_{abs,i}$ in Eq. (16) denotes the laser energy absorbed by phase i. The simplest way of distributing the absorbed laser energy, Q_{abs}, among phases, which we use here, is via

$$Q_{abs,i} = \frac{\rho_i}{\rho} Q_{abs}, \tag{18}$$

which represents an energy conservative distribution due to Eq. (8). As some materials, such as glass, are highly transparent in their solid state, we usually employ a distribution based on the phases' optical densities (e.g., the simulations presented in [30]), which we do not consider here for the sake of simplicity. For details on the calculation of Q_{abs}, cf. Section 2.5. The source term $S_{p,i}$ represents thermal-pressure coupling, again distributed in an energy-conserving manner among phases i, and reads

$$S_{p,i} = \frac{\rho_i}{\rho}\left(\frac{\partial(\rho k)}{\partial t} + \nabla \cdot (\rho \boldsymbol{u} k) + \frac{\partial p}{\partial t}\right) \tag{19}$$

with $k = 0.5(\boldsymbol{u} \cdot \boldsymbol{u})$. Heat conduction is modeled through

$$\frac{\partial\left(\rho c_p T\right)}{\partial t} = \nabla \cdot (\lambda \nabla T), \tag{20}$$

where λ, ρ, and c_p denote mixture thermal conductivity, density and specific heat capacity, respectively.

2.4. Phase change

Phase changes are modeled as transfer of mass and energy between two phases, making these processes inherently mass- and energy conservative. Furthermore, associated effects such as evaporative cooling or recoil pressure are an implicit result of the phase change model, as the transfer of energy, between two phases issues a change in temperature due to the latent heat separating the phase energies, and a mass transfer between two phases of different densities issues a change in volume, and thus pressure. The phase change model therefore only needs to yield how much mass (and associated energy) is to be exchanged between two phases depending on the local temperature and pressure.

2.4.1. Melting - Solidification

Melting and solidification are modeled as energy-based mass transfer. Denoting solid and liquid phase of a material undergoing melting or solidification with the subscripts s and l, respectively, we define the excess energy for melting or solidification, following the Enthalpy-porosity method [38], as

$$\Delta E_{melt} = H_s - \rho_s h_s(T_{solidus}), \tag{21}$$

$$\Delta E_{solidif} = \rho_l h_l(T_{liquidus}) - H_l, \tag{22}$$

where $h_i(T)$ denotes the specific heat at temperature T, and H_i is the energy of phase i (cf. Section 2.3). We then define the rate of melting and solidification as

$$\dot{\rho}_{l,m} = -\dot{\rho}_{s,m} = \rho_s \frac{\Delta E_{melt}}{L_{fus}} \frac{1}{\tau_{prop}}, \tag{23}$$

$$\dot{\rho}_{s,s} = -\dot{\rho}_{l,s} = \rho_l \frac{\Delta E_{solidif}}{L_{fus}} \frac{1}{\tau_{prop}}, \tag{24}$$

where L_{fus} is the latent heat of fusion and τ_{prop} is a propagation time. For pure elements, which undergo phase change at a dedicated melting temperature, we set $T_{liquidus} = T_{solidus} = T_{melting}$, whereas alloys typically feature a melting interval between $T_{solidus}$ and $T_{liquidus}$, within which the material is in a mushy state. In Fig. 4, the results for a simple one-dimensional Stefan problem are shown, for an alloy and a pure element of constant heat capacity (where, in this case, the melting temperature of the pure element equals the liquidus temperature of the alloy). The resulting solidification behavior is in agreement with metallurgical theory [39].

2.4.2. Evaporation - Condensation

We consider pressure-driven evaporation and condensation, as

$$\dot{\alpha}_v = |c_1|\left(p_{sat} - p_{ext}\right), \tag{25}$$

where α_v is the volume fraction of the vapor phase of a liquid–vapor phase pair l, v, undergoing evaporation or condensation, p_{sat} denotes the local saturation pressure, which is calculated according to the Clausius–Clapeyron law as

$$p_{sat}(T) = p_{ref} \exp\left(\frac{M L_{vap,eff}}{T_b R}\left(1 - \frac{T_b}{T}\right)\right), \tag{26}$$

with T_b, $L_{vap,eff}$, M and R denoting the material's boiling temperature, effective latent heat of vaporization, molar mass and the universal gas constant, respectively. The reduction of latent heat of vaporization from its reference value L_{vap} towards the critical point T_{crit} is modeled through the Watson equation [40] as

$$L_{vap,eff} = L_{vap}\left(\frac{T_{crit} - T}{T_{crit} - T_b}\right)^{0.38}. \tag{27}$$

Furthermore, p_{ext} denotes local external vapor pressure, and c_1 is a constant obtained from the Hertz–Knudsen model, related to the theoretical

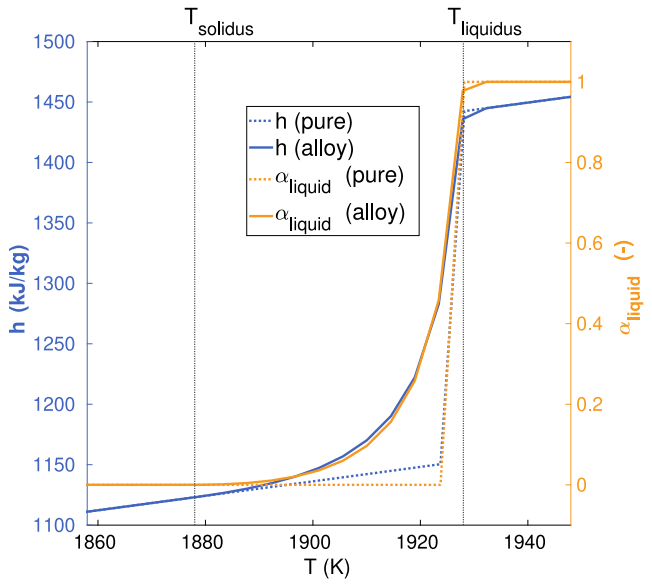

Fig. 4. Illustration of melting and solidification: Liquid volume fraction α_{liquid} and mass-specific energy h for an alloy featuring a melting interval, and a pure element, over Temperature T in a one-dimensional domain, where one boundary is set to $T_{hot} > T_{liquidus}$ and one boundary is set to $T_{cold} < T_{solidus}$. The results are plotted after a steady state is reached.

maximum instantaneous evaporation (or condensation, depending on the sign of the pressure difference in Eq. (25)) rate,

$$c_1 = \begin{cases} \varepsilon_e \sqrt{\frac{M}{2\pi RT}} \frac{1}{\xi \cdot \rho_{ref,l}(T)} \forall (p_{sat} > p_{ext}) \\ -\varepsilon_c \sqrt{\frac{M}{2\pi RT}} \frac{1}{\xi \cdot \rho_{ref,v}(T)} \forall (p_{sat} < p_{ext}) \end{cases}. \tag{28}$$

Here, subscripts l and v denote again the liquid and vapor phase of the material undergoing phase change and ξ is the thickness of the liquid-vapor interface. The model fully resolves the vapor phase and pressure increases, associated with evaporation, are directly linked to a reduction of the evaporation rate via an increase of p_{ext} in Eq. (25). Hence, no evaporation efficiency is needed and we set $\varepsilon_e = 1$. To account for the need for heterogeneous nucleation in condensation processes (or significant subcooling in the case of homogeneous nucleation) we set the condensation efficiency as $\varepsilon_c = \max(\sum \alpha_{cond}, 10^{-6})$, with $\sum \alpha_{cond} \leq 1$ denoting the sum of volume fraction of condensed matter, promoting condensation in the vicinity of condensed matter.

The change in ρ_l and ρ_v due to evaporation and condensation is then given by

$$\dot{\rho}_{l,e} = -\dot{\rho}_{v,e} = -\rho_l \dot{\alpha}_v^+, \tag{29}$$

$$\dot{\rho}_{l,c} = -\dot{\rho}_{v,c} = \rho_v \dot{\alpha}_v^-. \tag{30}$$

Note that here (and throughout this work), for any quantity x, x^+ and x^- are defined as

$$x^+ = \begin{cases} |x| & \forall x \geq 0 \\ 0 & \forall x < 0, \end{cases} \tag{31}$$

$$x^- = \begin{cases} 0 & \forall x \geq 0 \\ |x| & \forall x < 0. \end{cases} \tag{32}$$

2.5. Laser beam propagation and laser-material interaction

Only a brief overview on the beam propagation and laser-material interaction model is provided here, as the focus of this work lies on the fluid mechanical model. The main quantity of interest with respect to the fluid mechanical problem is the absorbed laser energy Q_{abs}, which is introduced as source term in the convective energy transport equation (16) and distributed among phases i in a manner equivalent to Eq. (18). We outline the model here at the example of a Gaussian laser intensity distribution, but in principle, any other type of intensity distribution for which an analytical or numerical (e.g., in the case of an experimentally measured laser beam profile) description is available can be treated analogously.

Utilizing the paraxial approximation and using cylindrical coordinates r, z, where z denotes the distance from the beam's focal point along its optical axis and r denotes the radial distance from the optical axis, the axisymmetrical intensity distribution $I(r, z)$ of a Gaussian laser beam is defined as [41]

$$I(r, z) = I_0 \left(\frac{w_0}{w(z)} \right)^2 \exp\left(\frac{-2r^2}{w(z)^2} \right), \tag{33}$$

where $I_0 = I(r = 0, z = 0)$ is the intensity at the focus, $w(z)$ is the beam's radius, with $w_0 = w(z = 0)$ being the focal radius, i.e., its minimum value. The radius is usually defined as the distance from the optical axis, at which $I = \exp(-2)$, i.e., approx. 86% of laser intensity lies within the radius. The axial profile of the radius is defined as [41]

$$w(z) = w_0 \sqrt{1 + \left(\frac{z}{z_R} \right)^2}, \tag{34}$$

where z_R is the Rayleigh length, reading

$$z_R = \frac{n\pi w_0^2}{M^2 \lambda_0}, \tag{35}$$

with n denoting the refractive index of the medium through which beam propagates, λ_0 denoting the vacuum wave length of the laser beam and M^2 being a quality factor describing the divergence of a real laser beam with respect to a perfect Gaussian beam. The case of $M^2 = 1$ is associated with a perfect Gaussian beam, and $M^2 > 1$ holds true for real beams. The radius of curvature of the propagating beam's wavefront, R_c, is defined as [41]

$$R_c(z) = z \left(1 + \left(\frac{z_R}{z} \right)^2 \right). \tag{36}$$

Utilizing the above beam description, we now define a unit vector $\boldsymbol{r}$ which is aligned with the laser beam's local direction of propagation, i.e., a unit vector normal to the wavefront of the laser beam, as

$$\boldsymbol{r}(r, z) = \frac{\cos(\theta)\boldsymbol{e}_z + \sin(\theta)\boldsymbol{e}_r}{\left|\cos(\theta)\boldsymbol{e}_z + \sin(\theta)\boldsymbol{e}_r\right|}, \tag{37}$$

with

$$\theta(r, z) = \arcsin\left(\frac{r}{R_c(z)} \right). \tag{38}$$

Up until initial incidence (first interaction between laser beam and condensed matter) we model beam propagation through a set of coupled steady-state Radiative Transport Equations (RTE) for laser intensity propagating through gaseous and condensed phases, respectively, I_g and I_{cond}, reading

$$\begin{aligned} \nabla \cdot \left(\boldsymbol{r} I_g \right) = & \\ & - \left(\zeta_g + \zeta_{plasma} \right) I_g \\ & - \frac{\left[\nabla \cdot \left(\boldsymbol{r} \alpha_{cond} \right) \right]^+}{\alpha_g} I_g \\ & + (1 - R) \frac{\left[\nabla \cdot \left(\boldsymbol{r} \alpha_{cond} \right) \right]^-}{\alpha_{cond}} I_{cond}, \end{aligned} \tag{39}$$

and

$$\begin{aligned} \nabla \cdot \left(\boldsymbol{r} I_{cond} \right) = & \\ & - \zeta_{cond} I_{cond} \\ & - \frac{\left[\nabla \cdot \left(\boldsymbol{r} \alpha_{cond} \right) \right]^-}{\alpha_{cond}} I_{cond} \\ & + (1 - R) \frac{\left[\nabla \cdot \left(\boldsymbol{r} \alpha_{cond} \right) \right]^+}{\alpha_g} I_g. \end{aligned} \tag{40}$$

Here, the steady-state assumption is motivated as the timescales of propagating light (at the speed of light) are much smaller than any thermo-fluid-mechanical timescales encountered within the process. Distinguishing between propagation through gaseous and condensed matter is necessary to consider partial reflection upon incidence on condensed matter, which is accounted for through the second and third source term on the RHS of Eqs. (39) and (40), respectively. The subscripts *cond* and *g* denote condensed and gaseous matter, respectively. Hence, $\alpha_{cond} = \sum_i^{N_{cond}} \alpha_i$ and $\alpha_g = \sum_i^{N_g} \alpha_i$ denote the volume fractions of condensed and gaseous matter, respectively. R denotes the material's reflectivity which is calculated based on the laser beam's incident angle using the Fresnel Equations [42],

$$R_S = \left| \frac{cos(\beta) - \underline{n}\sqrt{1 - sin^2(\beta)/\underline{n}}}{cos(\beta) + \underline{n}\sqrt{1 - sin^2(\beta)/\underline{n}}} \right|, \tag{41}$$

$$R_P = \left| \frac{\underline{n}cos(\beta) - \sqrt{1 - sin^2(\beta)/\underline{n}}}{\underline{n}cos(\beta) + \sqrt{1 - sin^2(\beta)/\underline{n}}} \right|, \tag{42}$$

$$R = \frac{R_S + R_P}{2}, \tag{43}$$

where $\underline{n} = n + i\kappa$ denotes the complex refractive index (consisting of refractive index n and extinction coefficient κ of the material, with i being the imaginary unit in this context), and β is the local angle of incidence, defined as $\beta = \arccos(\boldsymbol{n}_{cond} \cdot \boldsymbol{r})$, with $\boldsymbol{n}_{cond} = (\nabla \alpha_{cond})/(|\nabla \alpha_{cond}|)$. ζ_g and ζ_{plasma} are the absorptivity of gas and plasma, respectively, which are irrelevant for all cases investigated hereafter, as the absorptivity of vapor is set to zero in all subsequent test cases (as the gaseous phases' extinction coefficient κ is zero, and hence $\zeta_g = 0$), and no plasma forms, hence $\zeta_{plasma} = 0$. The interested reader is referred to [29] for more information on our plasma absorption model. The absorptivity of condensed matter, ζ_{cond} is modeled as

$$\zeta_{cond} = \frac{\sum_i^{N_{cond}} \alpha_i \left(\frac{4\pi\kappa_i}{\lambda_0} + \zeta_{i,NL} \right)}{\sum_i^{N_{cond}} \alpha_i}, \tag{44}$$

with $\zeta_{i,NL}$ denoting nonlinear absorption terms, which are not relevant for the materials and laser intensities investigated within this work, and are therefore being neglected hereafter for the sake of brevity. Hence, $\zeta_{i,NL} = 0$. Subsequent reflections after the initial incidence described by Eqs. (39)–(40) are accounted for through a ray tracing model. Within the ray tracing model, reflections at the $(\alpha_{cond} = 0.5)$-isosurface are calculated again angle-of-incidence-dependent using Eqs. (41)–(43). We finally obtain the absorbed laser energy from the input laser energy Q_{input} as $Q_{abs,I} = I_{cond} Q_{input} + Q_{abs,MR}$, with $Q_{abs,MR}$ denoting the amount of laser energy absorbed due to multiple reflections after initial incidence. The main advantage of splitting the beam propagation model into initial incidence following a set of RTEs and subsequently, a multiple reflection model, is the fact that the converging-diverging caustic of a laser beam can hence be accounted for. A pure ray tracing-based approach cannot account for the spatial change in beam divergence that is inherent to laser beams. On the other hand, neglecting multiple reflections would lead to unrealistically low absorption values, as in the case of a vapor depression or keyhole, or in the case of complex work piece geometries, multiple reflections are crucial for absorption and thus should not be neglected.

3. Numerical methods

The governing equations laid out in Section 2 are solved using a pressure-based, segregated Finite Volume Method. Details on the Finite Volume Method and its implementation in `OpenFOAM` can be found, e.g., in [43–46]. In this Section, we briefly lay out the numerical implementation and solution algorithm, with emphasis on parts that differ from the numerical implementation of the VoF solver `multiphaseInterFoam` [47,48] (the N-phase extension of the VoF solver `interFoam` [49]), which is the initial starting point for the numerical implementation of this work's model. The solution algorithm within one time step k of the transient solution procedure is summarized briefly in Table 1. Details regarding the most crucial steps of the solution procedure laid out in Table 1 are provided in Sections 3.1–3.5. Here, the superscript $k-1$ denotes the solution of the previous time step and superscript k denotes the solution of the current time step.

Table 1
Overview of solution algorithm within a time step k.

`for each timestep` k`, do:`	
	Update time increment Δt^k based on Eq. (45)
1	**Phase and energy advection**
1a	Solve Eq. (46) for $\rho^k_{i,conv}$ using $\boldsymbol{u}^{k-1}$ and α^{k-1}_i
1b	Solve Eq. (48) for $H^k_{i,conv}$ using $\boldsymbol{u}^{k-1}$, $Q^{k-1}_{abs,i}$, and $S^{k-1}_{p,i}$
1c	Calculate T^k_{conv} from H^k_{conv} as laid out in Section 3.2
1d	Phase-norming by minimizing Eq. (58) for $\alpha^k_{i,conv}$
2	**Beam propagation**
2a	Solve steady-state RTEs (39) and (40) iteratively using $\alpha^k_{i,conv}$, where in each iteration j, (39) is solved for I_g using I^{j-1}_{cond} and subsequently, (40) is solved for I_{cond} using I^j_g, until $\lvert(I_g + I_{cond})^j - (I_g + I_{cond})^{j-1}\rvert/(I_g + I_{cond})^{j-1} < \delta$
2b	Calculate $Q^k_{abs,I}$ from I^k_{cond}
2c	Calculate $Q^k_{abs,MR}$ via ray tracing algorithm using $Q^k_{abs,I}$ and $\alpha^k_{i,conv}$
2d	Calculate absorbed laser energy $Q^k_{abs} = Q^k_{abs,I} + Q^k_{abs,MR}$
3	**Heat conduction**
3a	Solve Eq. (20) for $T^k_{conduct}$ from T^k_{conv}
3b	Update $H^k_{i,conduct}$ from $T^k_{conduct}$ via Eq. (50)
4	**Phase change**
4a	Evaluate Eqs. (65)–(68) using $T^k_{conduct}$ and $H^k_{i,conduct}$
4b	Obtain ρ^k_i via Eq. (63)
4c	Obtain H^k_i and thus H^k via Eq. (70) and obtain T^k from H^k as laid out in Section 3.2
4d	Phase-norming by minimizing Eq. (58) for α^k_i
4e	Calculate Ψ^k from Eq. (62) using α^k_i
5	**PISO-Loop**
5a	Evaluate momentum predictor (75) using current values
5b	Solve pressure equation (77)
5c	Calculate $\boldsymbol{u}^k$ from Eq. (76) , calculate $S^k_{P,i}$ for use in timestep $k+1$
`end timestep`	

3.1. Courant number

As laser material processing is not always a convection-dominated problem (e.g., low intensity conduction-mode heating without melting, or wait times between scan tracks and layers in additive manufacturing via powder bed fusion, etc.), we limit the time increment by the maximum of convective and diffusive Courant numbers, ensuring

$$\mathrm{Co} = \max\left(\frac{\lambda \Delta t}{c_p \rho \Delta x^2}, \frac{|\boldsymbol{u}|\Delta t}{\Delta x} \right) \leq 1, \tag{45}$$

with λ, c_p, and ρ denoting mixture values of thermal conductivity, specific heat capacity, and density, respectively, and Δx denoting in this context the minimum dimension of a computational cell.

3.2. Phase and energy advection

We modify Eq. (9) by omitting the RHS terms related to phase change which are accounted for by explicit updating of ρ_i values in a separate step of the solution procedure denoted *Phase Changes* (step 4 in Table 1). Furthermore, we introduce an interface compression term following the widely used Weller scheme [45] to keep a sharp interface between condensed and gaseous phases, yielding

$$\frac{\partial \rho_i}{\partial t} + \nabla \cdot \left[\left(\boldsymbol{u}^{k-1} + \boldsymbol{u}_c^{k-1} \right) \rho_i \right] = 0, \tag{46}$$

where $\boldsymbol{u}_c$ represents an artificial interface compression velocity only active at the phase interface of condensed phases, defined as

$$\boldsymbol{u}_c = c_\alpha \boldsymbol{u} \frac{\nabla \alpha_{cond}}{|\alpha_{cond}|} \alpha_{cond}(1-\alpha_{cond}). \tag{47}$$

Here, $c_\alpha = 0$ corresponds to no interface compression, and $c_\alpha > 0$ introduces interface compression to counteract numerical diffusion. Usually, a value between 1 and 1.5 gives good results, in accordance with the findings of [45]. Throughout this work, a value of $c_\alpha = 1$ is chosen.

Convective transport of energy on a predetermined velocity field is ensured by solving Eq. (16) in the form

$$\frac{\partial H_i}{\partial t} + \nabla \cdot \left[\left(\boldsymbol{u}^{k-1} + \boldsymbol{u}_c^{k-1} \right) H_i \right] + S_{p,i}^{k-1} = Q_{abs,i}^{k-1}, \tag{48}$$

where again phase change-related sources on the RHS of Eq. (16) are omitted and accounted for in step 4. After solving Eq. (48) to obtain $H_{i,conv}^k$, we calculate the mixture energy after convection, H_{conv}^k, via Eq. (17). Then, following the manner of temperature recovery methods [39], we determine the distribution of T_{conv}^k through a Newton–Raphson iteration of the form

$$T_{n+1} = T_n + \frac{H - H_n}{C_{p,n}}, \tag{49}$$

where

$$H_n = \sum_{i=1}^{N} \rho_i h(T_n) \tag{50}$$

is the energy achieved by summation of phase energies at temperature T_n. Note that n denotes an iteration index within this context. The converged temperature value after the above iteration is then denoted $T_{conv}^k = T_{n,final}$, the temperature after convective heat transport.

3.3. Phase-norming

Each time we change the distribution of ρ_i (i.e., after solving Eq. (48) or after explicitly updating ρ_i in step 4), we need to obtain the distribution of phase volume fractions, α_i. We now utilize the relationship between ρ_i and α_i implicitly laid out in Section 2.2 to derive a numerical scheme to obtain α_i for any given ρ_i, which we call *phase-norming*.

We define a quantity

$$A_i = \frac{\rho_i}{\rho_{ref,i}}, \tag{51}$$

which is not to be confused with the volume fraction α_i. Here, $\rho_{ref,i}$ again denotes the temperature-dependent density of phase i at reference pressure p_{ref}. In contrast to a volume fraction, A_i is (in the general case) of non-unitary sum, i.e.,

$$\sum_{i=1}^{N} A_i \neq 1. \tag{52}$$

Two mechanisms can lead to $\sum A_i \neq 1$: Firstly, mass can enter or leave a control volume through convection, changing ρ_i, and secondly, $\rho_{ref,i}$ can change through phase changes or with temperature following thermal expansion or contraction. Generally, we encounter two different cases, which are schematically illustrated in Fig. 5: (a) expansion, characterized by $\sum A_i < 1$, and (b) compression, characterized by $\sum A_i > 1$. In Fig. 5, we consider two phases of different bulk moduli K_i, with $K_1 > K_2$. For the same pressure change Δp, phases with lower bulk modulus K_i experience a larger volumetric change ΔV (and vice versa). Phase-norming aims at finding the necessary local change in pressure Δp^* to fulfill

$$\sum_{i=1}^{N} A_i = 1, \tag{53}$$

i.e., the amount of expansion or compression required to achieve the given distribution of ρ_i. Using the definition of the bulk modulus, we introduce a relation between α_i and pressure p as

$$\frac{dp}{K_i} = -\frac{d\alpha_i}{\alpha_i}, \tag{54}$$

which is only valid for infinitesimal changes. For arbitrarily large changes we integrate over the isothermal change from state S_0 to state S_1,

$$\int_{S_0}^{S_1} \frac{dp}{K_i} = -\int_{S_0}^{S_1} \frac{d\alpha_i}{\alpha_i}. \tag{55}$$

To solve Eq. (55), we utilize the Tait equation, Eq. (15), yielding

$$\alpha_{i,1} = \frac{\alpha_{i,0}}{\sqrt[\gamma_i]{\frac{\Delta p}{B_{i,0}} + 1}}, \tag{56}$$

where $\alpha_{i,0}$ and $\alpha_{i,1}$ denote the volume fraction at states S_0 and S_1, respectively, where an isothermal change in pressure, Δp, was applied. We now utilize Eq. (56) to find Δp^* which is the necessary local change in pressure required to fulfill Eq. (53), as

$$\alpha_i = A_i \forall \left(\sum_{i=1}^{N} A_i = 1 \right). \tag{57}$$

We hence consider $\alpha_{i,0} = A_i$ and $\alpha_{i,1} = \alpha_i$, and aim at minimizing the term

$$\left(\sum_{i=1}^{N} \alpha_i \right) - 1 = \left(\sum_{i=1}^{N} \frac{A_i}{\sqrt[\gamma_i]{\frac{\Delta p}{B_i} + 1}} \right) - 1, \tag{58}$$

which can be directly computed for $N = 1$, but requires an iterative solution procedure for the general case of $N > 1$ with $K_i \neq K_j \; \forall i \neq j$. As the function in Eq. (58) is monotonic, we employ a bisection algorithm to find its minimum. Though showing slower convergence than, e.g., the Newton–Raphson method, it comes with the advantage of guaranteed convergence, independent of the starting value. The process of phase-norming is finished once the iterative root-finding of Eq. (58) has converged, i.e., $\left| \left(\sum_{i=1}^{N} \alpha_i \right) - 1 \right| \leq \delta$, with δ being a sufficiently small convergence tolerance. Then, $\Delta p = \Delta p^*$ and after finding Δp^*, we calculate a new value for the density-normed mixture compressibility, Ψ, as

$$\Psi = \frac{\psi}{\rho} = \frac{1}{K_{mixture}}, \tag{59}$$

where $K_{mixture}$ is not yet known, and for which we use the definition of the bulk modulus, as

$$\Psi = -\frac{d\left(\sum_i^N \alpha_i \right)}{\sum_i^N \alpha_i \cdot dp}, \tag{60}$$

and utilizing Eq. (56) yields

$$\Psi = -\frac{d\left(\sum_i^N \frac{A_i}{\sqrt[\gamma_i]{\frac{\Delta p \gamma_i}{K_i} + 1}} \right)}{\sum_i^N \alpha_i \cdot dp}. \tag{61}$$

Differentiation at $\Delta p = \Delta p^*$ leads to

$$\Psi^* = \Psi(\Delta p^*) = \sum_i^N \frac{\alpha_i}{\gamma_i(\Delta p^* + K_i/\gamma_i)}. \tag{62}$$

After phase-norming, we know the values of α_i (i.e., the volume fractions fulfilling Eq. (53)) which are used for tracking phase interfaces, e.g., as utilized in Eqs. (39)–(40) or Eq. (47), and for calculating volume-weighted material property values for the mixture of phases via Eq. (14). Furthermore, the value of $p^* = p_{ref} + \Delta p^*$ is used for pressure-based evaporation and condensation (cf. Section 3.4) and Ψ^* is used in the pressure equation within the PISO-loop (cf. Section 3.5).

3.4. Phase changes

The change of ρ_i due to the RHS terms in Eq. (9) is accounted for by explicitly updating ρ_i via

$$\rho_i^k = \rho_{i,conv}^k + \Delta\rho_{i,m}^k + \Delta\rho_{i,s}^k + \Delta\rho_{i,e}^k + \Delta\rho_{i,c}^k. \tag{63}$$

For melting and solidification, the propagation time τ_{prop} occurring in Eqs. (23) and (24) is simply taken as

$$\tau_{prop} = \frac{\Delta x_{LS}}{c_{sound}}, \tag{64}$$

with c_{sound} denoting the speed of sound and Δx_{LS} being the local Finite Volume cell length normal to the solid–liquid interface. The amount of mass molten or solidified within a time step is then calculated for any liquid–solid phase pair l, s undergoing phase change as

$$\Delta\rho_{l,m}^k = -\Delta\rho_{s,m}^k = \Delta t^k \rho_s^k \frac{\Delta E_{melt}}{L_{fus}} \frac{1}{\tau_{prop}}, \tag{65}$$

$$\Delta\rho_{s,s}^k = -\Delta\rho_{l,s}^k = \Delta t^k \rho_l^k \frac{\Delta E_{solidif}}{L_{fus}} \frac{1}{\tau_{prop}}, \tag{66}$$

and $\Delta\rho_{i,m}$ and $\Delta\rho_{i,s}$ are zero for all other phases. The amount of mass evaporated or condensed within a time step is calculated for any liquid-vapor phase pair l, v undergoing phase change as

$$\Delta\rho_{v,e}^k = -\Delta\rho_{l,e}^k = \rho_l^k \left(1 - \exp\left(-\frac{\Delta t^k c_1 (p_{sat} - p_{ext})}{1 + \frac{|c_1|\Delta t^k}{\tilde{\Psi}^*}}\right)\right), \tag{67}$$

$$\Delta\rho_{l,c}^k = -\Delta\rho_{v,c}^k = \rho_v^k \left(1 - \exp\left(-\frac{\Delta t^k c_1 (p_{sat} - p_{ext})}{1 + \frac{|c_1|\Delta t^k}{\tilde{\Psi}^*}}\right)\right), \tag{68}$$

where c_1 is calculated according to Eq. (28), with ξ simply taken as the local Finite Volume cell length normal to the liquid-vapor interface. To account for the possibility of newly created vapor to escape into the vicinity, due to the pressure level surrounding the liquid-vapor interface, we employ a time step- dependent limiter in the above term using a locally averaged compressibility, $\tilde{\Psi}$, calculated within a computational cell j as

$$\tilde{\Psi}_j = \frac{\sum_{m \in U(j)} V_m \Psi_m}{\sum_{m \in U(j)} V_m}, \tag{69}$$

with $U(j)$ denoting all cells that share a face with cell j.

When updating the values of ρ_i following phase change, we also transfer the respective fraction of energy H_i associated with $\Delta\rho_i$ between the phases involved in the phase change process via

$$H_i^k = H_{i,conduct}^k + \Delta H_{i,m}^k + \Delta H_{i,s}^k + \Delta H_{i,e}^k + \Delta H_{i,c}^k, \tag{70}$$

where

$$\Delta H_{i,m}^k = \Delta\rho_{i,m}^k \; h_i(T_{conduct}^k), \tag{71}$$

$$\Delta H_{i,s}^k = \Delta\rho_{i,s}^k \; h_i(T_{conduct}^k), \tag{72}$$

$$\Delta H_{i,e}^k = \Delta\rho_{i,e}^k \; h_i(T_{conduct}^k), \tag{73}$$

$$\Delta H_{i,c}^k = \Delta\rho_{i,c}^k \; h_i(T_{conduct}^k). \tag{74}$$

3.5. PISO-loop

To establish pressure–velocity coupling we employ a PISO algorithm (Pressure Implicit with Splitting of Operators, cf. [45] for a detailed description), where we use a typical decomposition of the matrix form of the momentum equation (2) as

$$\boldsymbol{A}\boldsymbol{u} - \boldsymbol{H} \equiv \frac{\partial(\rho \boldsymbol{u})}{\partial t} + \nabla \cdot (\rho \boldsymbol{u}\boldsymbol{u}) - \nabla \cdot \boldsymbol{\tau} - \boldsymbol{S_D} + \boldsymbol{S_B} - \boldsymbol{S_S}, \tag{75}$$

and thus,

$$\boldsymbol{A}\boldsymbol{u} - \boldsymbol{H} = -\nabla p. \tag{76}$$

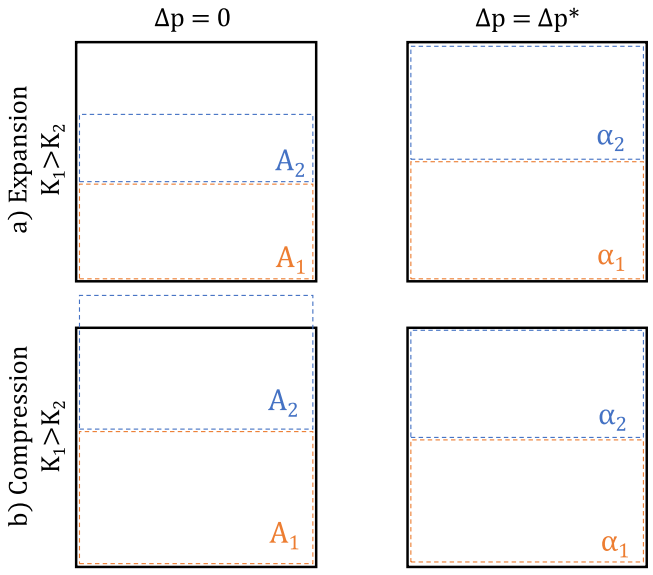

Fig. 5. Schematic illustration of phase-norming within the MoF method for the example of two phases of different bulk moduli in a control volume (black outline). Depending on the value of $\sum A_i$ within the control volume, we distinguish between expansion (top) and compression (bottom). At a given pressure change Δp, phases with a lower bulk modulus experience a larger volumetric change (and vice versa).

A pressure equation is constructed following the approach of [50], making use of the continuity Eq. (1), as

$$\underbrace{\nabla \cdot \left(\boldsymbol{A}^{-1}\boldsymbol{H}\right) - \nabla \cdot \left(\boldsymbol{A}^{-1}\nabla p\right)}_{\nabla \cdot \boldsymbol{u}} = \frac{\partial(\Psi^* p)}{\partial t} + \nabla \cdot \left(\Psi^* \boldsymbol{u} p\right) - p\nabla \cdot \left(\Psi^* \boldsymbol{u}\right), \tag{77}$$

where we utilize the fact that

$$\frac{1}{\rho}\frac{\partial \rho}{\partial p} = \Psi. \tag{78}$$

4. Results

To assess the accuracy and universality of the model, test cases of increasing complexity are simulated, starting with academic problems and moving on to more complex problems of laser material processing. It is worth noting that, for solving the problems presented hereafter, the exact same model is used, only changing input properties such as the number of phases and their respective thermophysical properties, the domain geometry and its discretization, and initial and boundary conditions. Spatial discretization is, in all subsequent cases (except Case 3), achieved through meshing with a conformal, purely hexahedral mesh of unitary aspect ratio. In two cases (Sections 4.4 and 4.5) mesh refinement is employed, by iteratively splitting a hexahedral Finite Volume into eight smaller volumes of equal size.

4.1. Case 1: Single-phase shock tube

Sod's one-dimensional shock tube problem [51] is simulated and compared to the results obtained with the density-based compressible flow solver `rhoCentralFoam` [52], in its native `OpenFOAM-6` version [47], which is dedicated to this exact type of problem. Initial conditions, material properties, geometry and spatial and temporal discretization are listed in Table 2 and are identical for both the simulations with this work's model and `rhoCentralFoam`. The constant time step was kept identical for both the fine and coarse mesh, leading to a very low Courant number for the coarse mesh, but the emphasis was put on keeping all parameters unchanged when comparing the coarse and fine solution. Initial values in the left and right part of the domain are denoted by subscripts 1 and 2, respectively. The simulation

Table 2
Single-phase shock tube: Initial conditions, material properties and discretization.

Property	Value	Unit
Initial conditions		
Pressure p_1	$1 \cdot 10^5$	Pa
Pressure p_2	$0.1 \cdot 10^5$	Pa
Temperature T_1	348.432	K
Temperature T_2	278.746	K
Velocity $u_1 = u_2$	0	m s^{-1}
Material properties		
Specific heat capacity c_p	1004.5	m^2 s^{-2} K^{-1}
Molar mass M	$28.96 \cdot 10^{-3}$	kg mol^{-1}
Thermal conductivity λ	0	kg m s^{-3} K^{-1}
Synamic viscosity μ	0	Pa s
Density ρ	*ideal gas law*	kg m^{-3}
Heat capacity ratio c_p/c_v	1.4	–
Bulk modulus K	$1 \cdot 10^5$	Pa
Domain and discretization		
Domain length l	10	m
Cell size Δx_c (coarse)	0.1	m
Cell size Δx_f (fine)	0.01	m
Time step Δt	$1 \cdot 10^{-6}$	s

is performed on a coarse mesh and a fine mesh. No-slip conditions for u, and zero gradient conditions for T, p and ρ_i are employed at the domain boundaries.

The spatial distributions of u, T, p and ρ at time $t = 0.07$ s are shown in Fig. 6, where reasonable agreement between the two solvers is achieved on the coarse mesh, and almost perfect agreement is reached on the fine mesh.

4.2. Case 2: Two-phase shock tube

A one-dimensional two-phase shock tube (filled with pressurized air and water) is simulated, in the configuration as investigated by Koch et al. [36], which can be seen as a one-dimensional model for cavitation bubble expansion. The purpose of this test case is to validate the model's ability of resolving compressible flow scenarios involving two fluids of different density and compressibility, where discontinuities need to be resolved and a segregated interface needs to be accurately captured. Initial conditions, material properties, geometry and spatial and temporal discretization are listed in Table 3. It is noted that the initial temperature values are chosen to match the initial density of air used by [36] via the ideal gas law, and is set equal in both sides of the domain as the liquid's density is modeled constant with respect to temperature (the liquid density's dependence on pressure follows the Tait equation, cf. Section 2.2). The results obtained at $t = 0.8$ µs are compared to the exact solution of [36] and provided in Fig. 7, exhibiting very good agreement.

4.3. Case 3: Converging-diverging nozzle

In the context of laser material processing, supersonic flows and their interaction with liquid material are often encountered. One example for such a process is continuous fiberizing by laser melting and supersonic dragging, where continuous glass nanofibers are produced [53]. Instabilities in the supersonic gas jet, such as shock waves, can cause oscillations of the filament. Another example is the widely employed process of laser cutting, where a supersonic jet is used to remove liquid metal during the process of cutting, and interactions between the jet and the material have a great influence on the resulting process outcome [54]. Thus, to accurately model such processes, the simulation model must be able to accurately predict real-world gas flows including shock waves. Quintero et al. [55] experimentally investigated the supersonic jet produced by a converging-diverging nozzle that is used in a continuous fiberizing process and simulated the jet

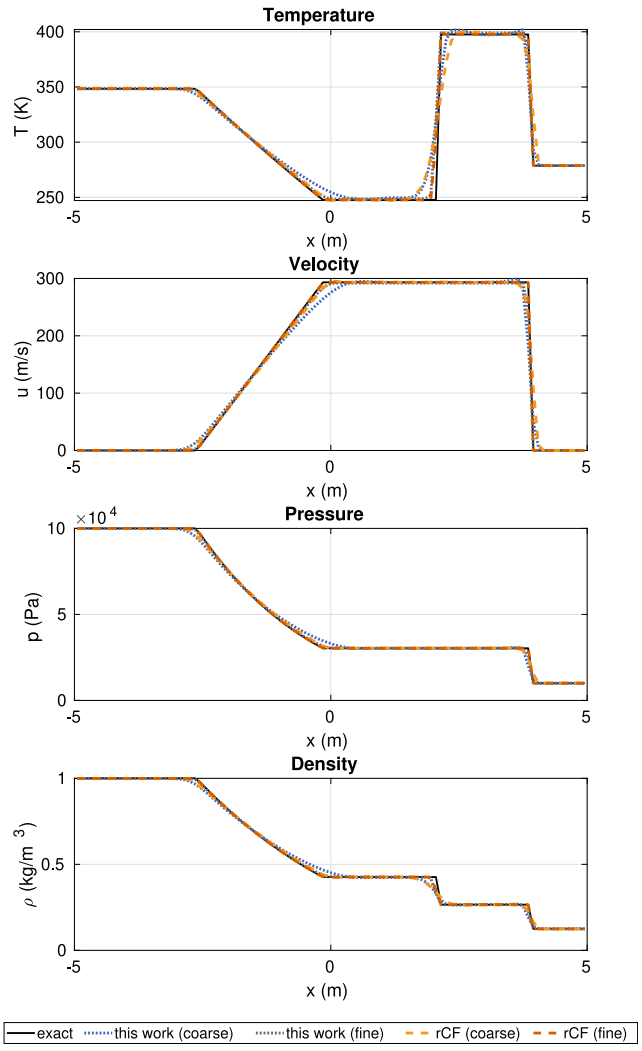

Fig. 6. Shock Tube: Comparison of exact solution and simulation results at $t = 0.007$ s on coarse and fine mesh, obtained with this work's model and with `rhoCentralFoam` (denoted rCF), respectively.

using different `OpenFOAM` solvers dedicated to single-phase supersonic flow simulations. The problem is simulated with this work's model, and compared to the experimental results of [55]. A sketch of the nozzle used in experiment, and the meshed geometry of the model are shown in Fig. 8. The diameter of the nozzle throat and nozzle exit are $D_t = 5$ mm and $D_e = 5.5$ mm, respectively. As turbulence plays a significant role, we include turbulence effects by including a turbulent viscosity μ_t in the viscous stress tensor of Eq. (2), which we calculate from the standard k-ϵ model. The mesh is equivalent to that reported in [55] (axisymmetric wedge type covering 2.5° of the three-dimensional physical domain, $\Delta x = 50$ µm). The material is treated as an ideal gas with a molar mass of $M = 28.9$ g mol^{-1} and a heat capacity ratio of $c_p/c_v = 1.4$. Thermophysical properties, initial conditions and boundary conditions used in the simulation are also equivalent to those reported in detail in [55], and therefore not repeated here.

The results in terms of density, ρ, and its gradient, grad(ρ) are compared to experimental observations in Fig. 9, showing good agreement in terms of shock wave structures and locations. The experimental results were obtained through digital holographic interferometry, utilizing the proportional correlation of optical phase and air density. For visualization in Fig. 9, the values are normalized by mapping to greyscale values through $[\min, \max] \rightarrow [0, 1]$.

Table 3
Two-phase shock tube: Initial conditions, material properties and discretization.

Property	Value	Unit
Initial conditions		
Pressure p_1	$1.5 \cdot 10^8$	Pa
Pressure p_2	$1 \cdot 10^5$	Pa
Temperature $T_1 = T_2$	2374.8	K
Velocity $u_1 = u_2$	0	m s^{-1}
Volume fraction $\alpha_{water,1}$	0	–
Volume fraction $\alpha_{water,2}$	1	–
Volume fraction $\alpha_{air,1}$	1	–
Volume fraction $\alpha_{air,2}$	0	–
Material properties (water)		
Density ρ	998.2061	kg m^{-3}
Specific heat capacity c_p	4184	m^2 s^{-2} K^{-1}
Thermal conductivity λ	0	kg m s^{-3} K^{-1}
Kinematic viscosity ν	$3.645 \cdot 10^{-7}$	m^2 s^{-1}
Surface energy σ	0	N m^{-1}
Bulk modulus K	$2.178 \cdot 10^9$	Pa
Material properties (air)		
Density ρ	*ideal gas law*	kg m^{-3}
Heat capacity ratio c_p/c_v	1.4	–
Molar mass M	$28.96 \cdot 10^{-3}$	kg mol^{-1}
Specific heat capacity c_p	1004.5	m^2 s^{-2} K^{-1}
Thermal conductivity λ	0	kg m s^{-3} K^{-1}
Kinematic viscosity ν	0	m^2 s^{-1}
Surface energy σ	0	N m^{-1}
Bulk modulus K	$1 \cdot 10^5$	Pa
Domain and discretization		
Domain length l	$3 \cdot 10^{-3}$	m
Cell size Δx_c (coarse)	$2 \cdot 10^{-6}$	m
Cell size Δx_f (fine)	$2 \cdot 10^{-7}$	m
Time step Δt	$1 \cdot 10^{-10}$	s

4.4. Case 4: Stationary illumination of Ti-6Al-4V bare plate

The stationary laser illumination experiment of Cunningham et al. [56] is simulated. In this experiment, in-situ X-ray tomography was used to observe stationary laser beam melting and evaporation on a Ti-6Al-4V bare plate. This experiment has previously been used for validating simulation models by, e.g., Wang et al. [12], Yu and Zhao [10], and Flint et al. [16] as it is particularly suited for this type of validation due to the high spatial and temporal resolution of the reported data. The problem is also interesting per se, as it features conditions (material, laser power and spot size) encountered in industrial additive manufacturing processes, where an understanding of the onset and evolution of a vapor depression and subsequently a keyhole (deep vapor depression of high aspect ratio), as well as its periodic growth and collapse, is important.

Although a Gaussian intensity distribution was provided by the laser source in the experiments of [56], an optical fiber was used to transport the laser light to the scanning head, which due to multiple reflections within the fiber transforms the beam profile into a tophat-like distribution [57]. As no intensity distribution measurements were available, a distribution following measurements conducted by Kaplan [57] was used and scaled to achieve the 140 μm and 95 μm beam diameters (using the $1/e^2$-diameter definition) reported by [56]. The use of a perfect Gaussian intensity distribution leads to higher drill rates and an earlier onset of fluctuations, as observed, e.g., in the simulations of Wang et al. [12]. The used computational domain and mesh are shown in Fig. 10. The mesh consists of 462 016 hexahedral cells, with the largest cell size (at the domain bottom) being Δx_{coarse} = 25 μm, and the smallest cell size (in the zone of interest, where beam propagation, melting, evaporation, etc. occur) being Δx_{fine} = 6.25 μm. The experimental setup is reproduced, using a domain width of 400 μm in $\vec{e}_x$-direction, with a zero gradient thermal boundary condition at the domain boundaries initialized with metal below a height ($\vec{e}_y$-direction) of −0.4 mm, and a fixed value (T = 300 K) thermal boundary condition at the lower domain boundaries, to model the clamping setup used in the experiment. Domain boundaries initialized with ambient gas are

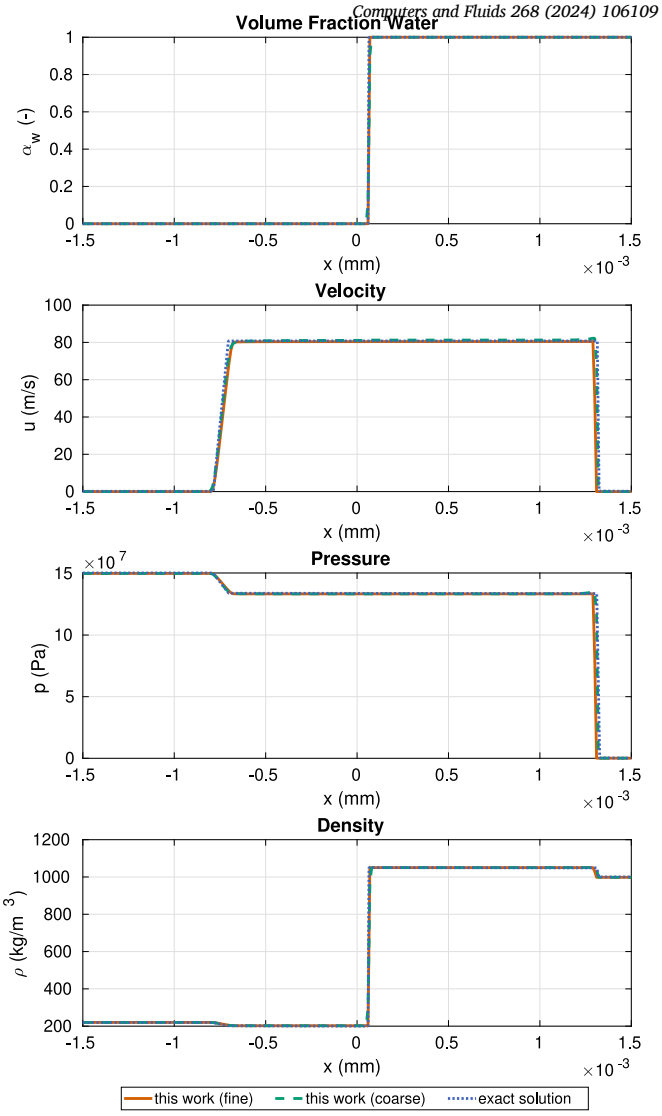

Fig. 7. Two-Phase Shock Tube: Comparison of simulation results at $t = 0.8$ μs obtained with this work's model and the exact result reported by Koch et al. [36].

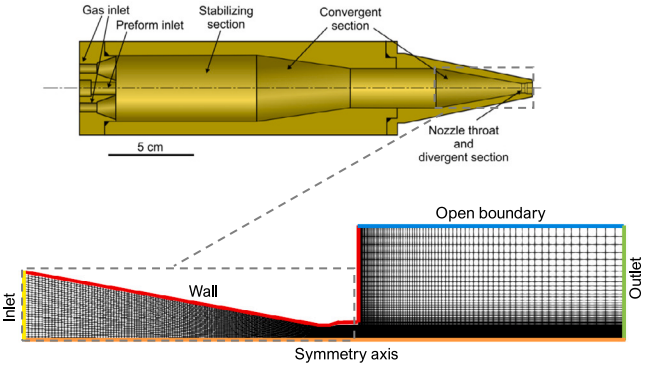

Fig. 8. Converging-Diverging Nozzle: Schematic drawing of nozzle geometry used in experiment (reprinted from [53]. ©The Authors, some rights reserved; exclusive licensee AAAS. Distributed under a CC BY-NC 4.0 license http://creativecommons.org/licenses/by-nc/4.0/. Reprinted with permission from AAAS.) and two-dimensional view of axisymmetrical wedge-type mesh employed in the region of interest.

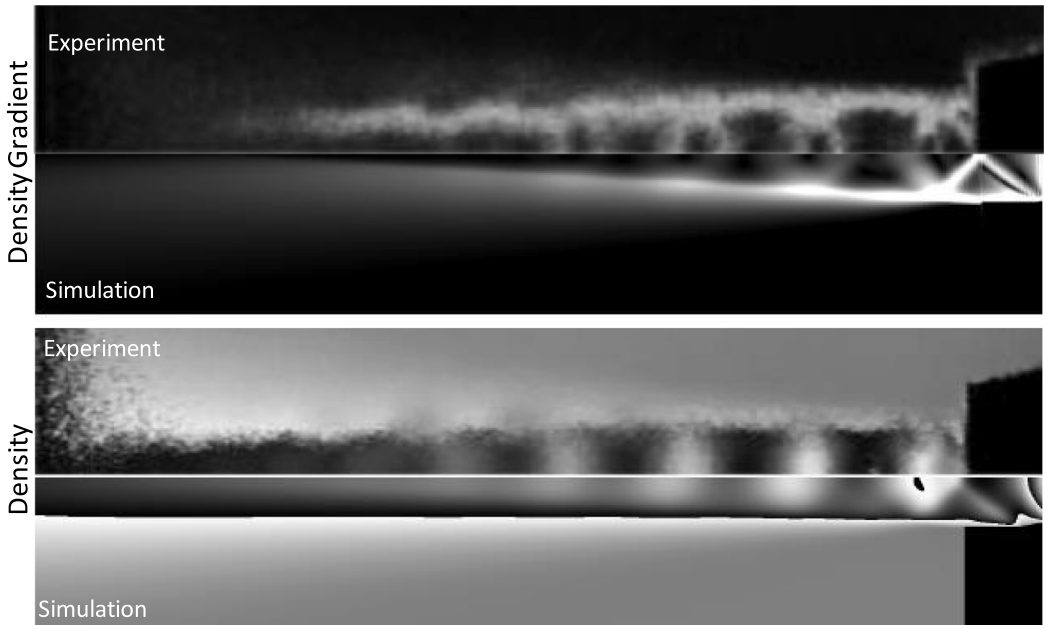

Fig. 9. Converging-Diverging Nozzle: Comparison of grad(ρ) (top) and ρ (bottom) between simulation and experiment of Quintero et al. [55] for inlet pressure of p_{in} = 3.5 bar. Experimental ρ is calculated from measured optical density.

modeled as inlet/outlet. The used material properties are provided in Appendix.

Following the approach of [12], we shifted the time values reported by [56] in Figs. 11 and 12 such that the first evolution of a vapor depression is matched between experiment and simulation, to account for a non-synchronization between switching on the laser and starting the recording. Fig. 11 shows the evolution of keyhole depth over time for two different laser spot sizes, where especially with the larger spot size two distinct regimes can be identified, i.e., the initial steady growth of the keyhole, followed by a sudden onset of violent fluctuations, accompanied by an increase in drill rate. The initial fluctuations deviating from the mean drill rate in the first part of the process (at $t < 0.75$ ms) are within the size of the computational cells, and can therefore be neglected. At a distinct point, the evaporation-induced recoil pressure suddenly outweighs the surface tension force at the liquid-vapor interface, resulting in a sudden increase in keyhole depth, reaching towards the bottom of the meltpool. The drilling process thus gains efficiency, as the melt pool also increases in depth, associated with a change in melt pool shape from hemispherical to conical. In Fig. 12, the transition from steady keyhole growth to deep fluctuations, and keyhole shape irregularities and keyhole collapse at a later stage are compared to the experimental images of [56], showing good agreement. In Fig. 13, the process using a smaller spot size is shown at three different stages, i.e., initial onset and steady growth of vapor depression, and violent keyhole fluctuations involving keyhole collapse at two different stages. For this used spot size, no experimental footage was available, but the good agreement of keyhole depth evolution shown in Fig. 11 suggests that the results in Fig. 13 are correct. Fig. 14 provides a detailed view of the result of the 95 µm spot size case at t = 260 µs, where the keyhole tip has just collapsed, and the remaining bubble is partly within the solid and within the melt pool, while collapsing. In the left view of Fig. 14, the bubble collapse can be seen through the low pressure at the bubble wall, and the liquid flow velocity vectors being oriented towards the bubble. Meanwhile, the evaporation-induced recoil pressure can be seen in the form of high pressure regions at the keyhole wall, with velocity vector at the upper part of the keyhole being oriented upwards, which is due to entrainment by the metal vapor escaping the keyhole. In the right view of Fig. 14, the flow structures of metal vapor escaping the keyhole, with a recirculation zone on the side (vortex structure). Furthermore, $\sum A_i$ is plotted, which can be seen as a measure of compression (cf. Section 3.3), where the bubble at the melt pool bottom is characterized by $\sum A_i < 1$, as most metal vapor has already condensed (cf. Fig. 13), and thus the remaining gas is expanded, resulting in a low pressure. Vice versa, the lower part of the keyhole, where new metal vapor is created through evaporation, but cannot escape freely, $\sum A_i > 1$ due to the additional volume of (compressed) metal vapor. The phenomena shown in Fig. 14 shall merely serve as an example of the various insights that can be gained from the here-presented model.

4.5. Case 5: Keyhole welding of copper

Keyhole welding of Cu-ETP is simulated and the results are compared to the corresponding in-situ synchrotron X-ray observations at high spatial and temporal resolution conducted by Schricker et al. [58]. The problem is well suited as a validation case because it features a process of high industrial relevance, e.g., for the manufacturing of electric vehicle components. Another benefit of this comparison results from the high resolution of reported experimental data, which allows to test the sensitivity of the laser-fluid interaction of the model and the coupling between different forces. The problem is also interesting per se, as it gives insight into the high dynamicity of the process and aids in gaining process understanding. Within this case, the laser power is 3.5 kW, with a spot size of 90 µm and a feedrate of 10 m/min. The used material properties are provided in Appendix. The computational domain and mesh are shown in Fig. 15, where initially, hexahedral cells of cell size $\Delta x_{initial}$ = 200 µm are used, which are dynamically refined up to 3 times during the simulation, depending on the presence of laser energy and liquid, leading to a local minimum cell size of Δx_{fine} = 25 µm.

In agreement with the experiment, the keyhole is in general quite narrow, but with increasing depth, irregularities increase (mainly in the form of bulges and waves). Although these are much more pronounced at the keyhole back wall, slight irregularities can also be seen on the keyhole front wall. Different forms of bulges can be observed at the keyhole back wall, of which the largest bulges form at the bottom and in the upper part of the keyhole. Some process snapshots showing extreme cases of lower, upper and minimum bulging are compared to the respective experimental observations of [58] in Fig. 16. To also enable a quantitative comparison, the keyhole shape is characterized by t_a and

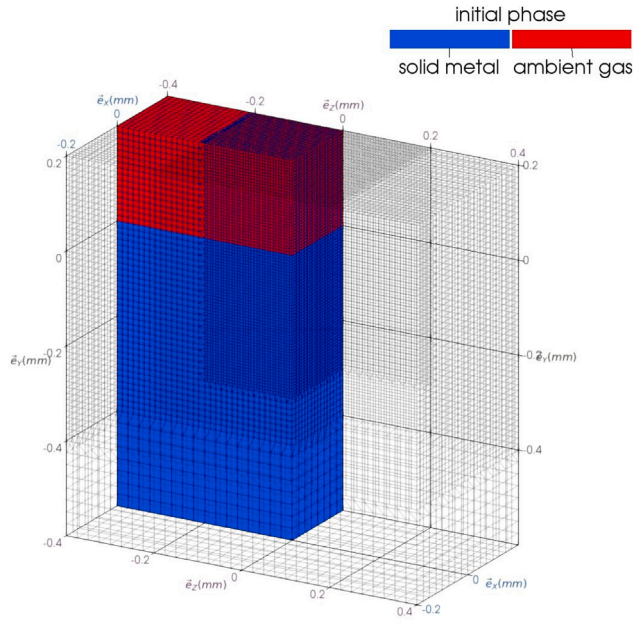

Fig. 10. Stationary Illumination of Ti6Al4V bare plate: Computational domain, mesh and initial phase distribution. To show the mesh refinement, the domain is cut in this image along the $\vec{e}_x$- and $\vec{e}_z$-direction, showing only a quarter of the initialized fields.

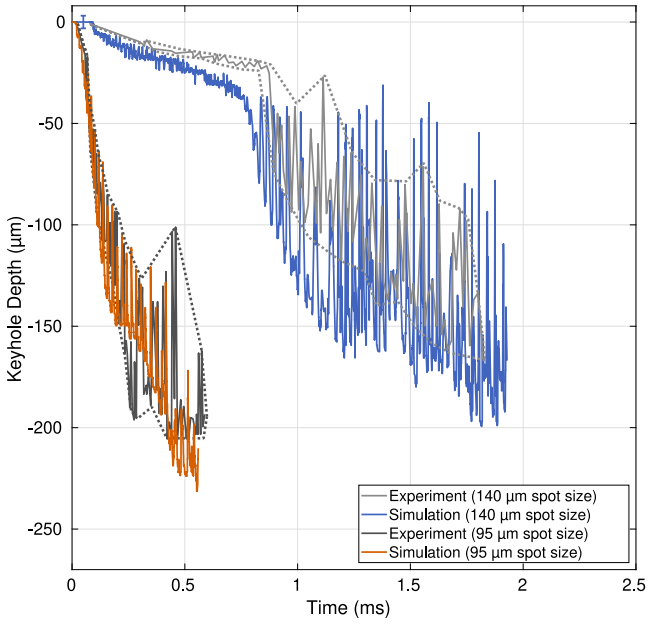

Fig. 11. Stationary Illumination of Ti6Al4V bare plate: Comparison of vapor depression (keyhole) depth obtained with this work's model and in experiment by Cunningham et al. [56], respectively. P_{Laser} = 156 W, d_{Laser} = [95 µm, 140 µm]. The cell size used in the simulations is given in the form of an errorbar in the initial flat part of the 140 µm spot size line.

t_d, referring to the depth position of the largest bulge and the keyhole depth, respectively, and a and d referring to the size of the bulge and the keyhole aperture at the top surface, respectively. The thus obtained dimensionless geometry parameters show good agreement, except for a/d in the bottom bulge scenario, where the keyhole aperture size is slightly larger in the simulation, most likely due to the wave at the upper keyhole back wall having already traveled further upwards in the simulation than in the respective experimental image. The occurrence of the maximum upper bulge (at t = 11.35 ms in simulation) is linked to a large wave of liquid being expelled backwards at the top of the rear keyhole wall in both simulation and experiment. The various dynamic processes reported in [58] can also be seen in the simulation. In Fig. 17, the ejection of spatter, associated with a subsequent increase in keyhole aperture is shown. Interestingly, the formation of a pore through pinch-off of the upper bulge can be seen in experiment and simulation (at t = 6.85 ms). The pore later re-attaches to the keyhole and is thus not preserved both in simulation and experiment. Another interesting dynamic process that is observed both in simulation and experiment is shown in Fig. 18, where, following a spatter ejection event, a wave on the keyhole rear wall travels upwards, but then is not ejected but stays attached to the melt pool and travels backwards.

This case provides many more possibilities for qualitative and quantitative comparison, and the simulation can be effectively used to explain the physical cause–effect relationships leading to the experimentally observed phenomena, which is outside the scope of this work. Currently ongoing work is dedicated to in-depth analysis of copper welding using the here-presented model, and the results will be presented in a forthcoming publication.

5. Discussion

The main novelty of the MoF approach is, that instead of advecting a marker function to calculate mass distributions from this marker, like in the VoF approach, we directly advect the conserved quantities of mass and energy, making the approach mass- and energy-conservative. Furthermore, this enables an intuitive inclusion of compressibility in the model, and makes the handling of phase changes straightforward. The approach, however, suffers from the problem that an artificial flux-based interface sharpening method needs to be employed in Eq. (9), because we do not advect a bounded volume fraction, but a local mass density. Typical VoF solvers can easily (at least for two phases) adopt novel interface sharpening methods such as `isoAdvector` [59], which is based on geometric interface reconstruction. Apart from this drawback, the framework proves to be well-suited to handle compressible segregated multiphase scenarios involving phase change. Especially when considering processes involving evaporation, and the thus induced recoil pressure acting on the liquid (which is the case even for low-power processes such as additive manufacturing by laser-based powder bed fusion, as shown by [56]), the recoil pressure does not need to be explicitly modeled. Therefore, no model fine tuning to a specific application through, e.g., a recoil pressure scaling constant is needed. The sudden change from a steadily growing vapor depression to violent fluctuations seen in Fig. 11 happens as soon as the recoil pressure is outweighing the surface tension force at the liquid-vapor interface. Here, the recoil pressure does not only depend on the degree of superheating of the liquid, but also on the geometry of the vapor depression and how well the newly produced vapor can escape the depression. Therefore, including the vapor phases and their compressibility in the model enhances the possibilities of drawing conclusions regarding the physical cause–effect relations at play and thus gain process understanding. The same holds true for the copper welding case investigated in Section 4.5. The chaotic nature of the underlying coupled multi-physical process leads to a broad range of irregularities, in a seemingly steady-state process.

The physics-based approach used in this work furthermore highlights the need for accurate temperature-dependent thermophysical and optical material properties in the liquid and gaseous state, as their influence on the process outcome can be high, but data in the literature is scarce and scattered, especially at the high temperatures encountered in laser-material processing.

The simulations presented in Section 4.4 took approximately 24 h (for the large spot size configuration) on 10 cores (Intel® Xeon™ E5-2690 processor). The use of dynamic mesh refinement would speed up the calculations, but was omitted in this case to allow for easier reproducibility of the results. The simulation presented in Section 4.5 took approximately 20 h per 1 mm of simulated weld bead length on 20 cores (Intel® Xeon™ E5-2690 processor). While the spatial resolution (and thus also the required temporal resolution) employed in the

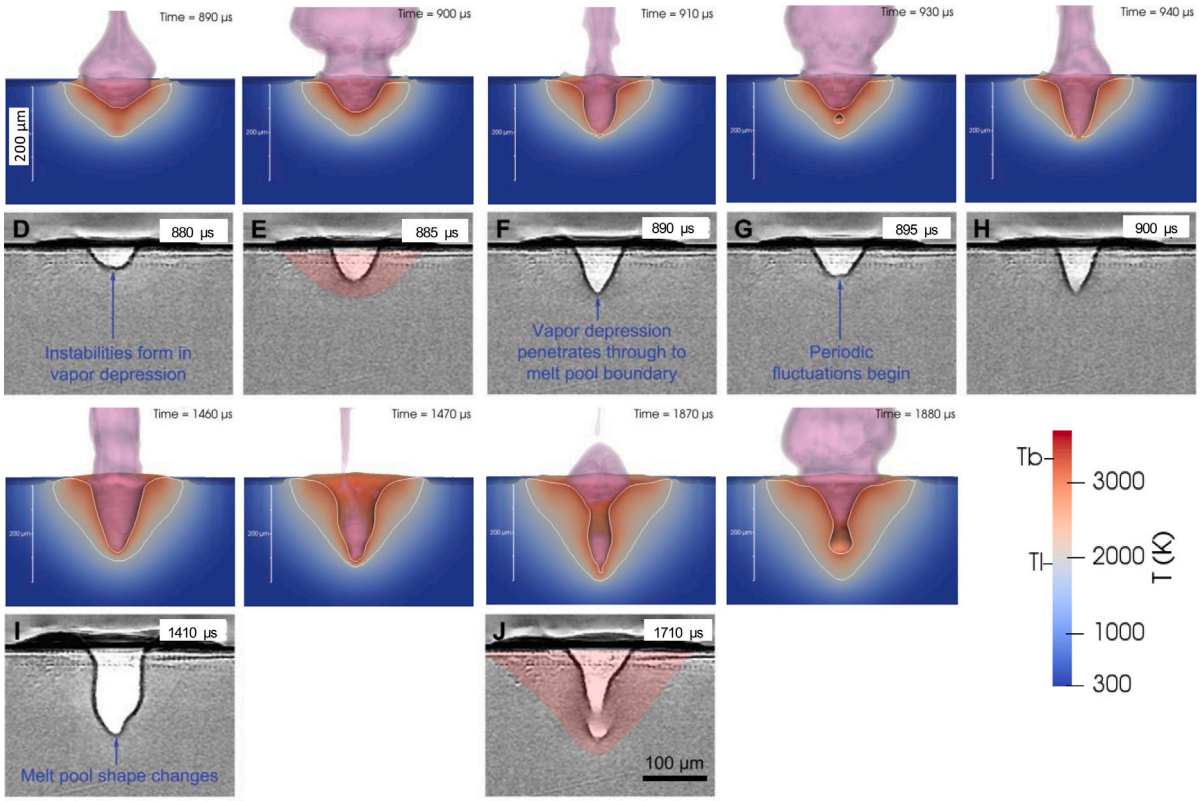

Fig. 12. Stationary Illumination of Ti6Al4V bare plate: P_{Laser} = 156 W, d_{Laser} = 140 µm. Simulation compared to experiment, showing transition from steady keyhole growth to violent fluctuations (experimental frames D-H) and keyhole collapse at later stage (experimental frames I-J). Cut through domain half, showing condensed matter colored by temperature, and contour surfaces of metal vapor (purple) at different α_{vap}-iso-values within $0.5 < \alpha_{vap} < 1$, white line denotes $\alpha_{liquid} = 0.5$. Experimental images are from Cunningham et al. [56]. Reprinted with permission from AAAS.

here-presented cases is very high to capture the highly dynamic phenomena observed experimentally, many practical applications of the here-presented framework allow for lower resolution. As an example, the here-presented model was used in [26] to simulate 30 mm of overlap welding of two 1 mm steel sheets (in good agreement with experimental results), where one simulation took approximately 12 h on an eight-core desktop computer.

6. Conclusion

A novel multiphase mixture model for laser-based material processing was presented. It is capable of accurately predicting compressible multiphase flows involving phase changes. The main difference over the Volume-of-Fluid method is that, instead of a marker function, the conserved physical quantities of mass and energy are tracked. An evaporation and condensation model that considers the created vapor and the arising pressure is derived, omitting the need of explicit recoil pressure calculation and model parameters for evaporation efficiency. The accuracy of the model and its numerical implementation was tested on one- and two phase shock tube scenarios, yielding very good results when compared to the respective analytical solutions or that of a state-of-the-art dedicated solver. The model's versatility and applicability to real-world laser material processing scenarios was showcased by simulating two different experiments where fine spatial and temporal data on the dynamic process is available. The results show excellent agreement with experimental observations and give detailed insight into the physical phenomena at play in additive manufacturing and welding processes.

Ongoing and future work focuses on the inclusion of further multiphysical aspects to the here-presented framework, such as solid mechanics and crystallographic grain growth, as well as a highly parallelizable Lagrangian particle-based implementation of the laser beam propagation and laser-material interaction model.

CRediT authorship contribution statement

Constantin Zenz: Conceptualization, Methodology, Software, Validation, Investigation, Visualization, Writing – original draft, Writing – review & editing. **Michele Buttazzoni:** Methodology, Software, Validation, Writing – review & editing. **Tobias Florian:** Validation, Investigation, Writing – review & editing. **Katherine Elizabeth Crespo Armijos:** Investigation, Visualization, Writing – review & editing. **Rodrigo Gómez Vázquez:** Methodology, Software, Supervision, Writing – review & editing. **Gerhard Liedl:** Supervision, Writing – review & editing. **Andreas Otto:** Conceptualization, Methodology, Supervision, Resources, Project administration, Funding acquisition, Writing – review & editing.

Declaration of competing interest

The authors declare that they have no known competing financial interests or personal relationships that could have appeared to influence the work reported in this paper.

Data availability

Data will be made available on request.

Acknowledgments

C. Zenz gratefully acknowledges funding through the TU Wien Doctoral School, within the Doctoral College "DigiPhot". The authors acknowledge TU Wien Bibliothek, Austria for financial support through its Open Access Funding Programme.

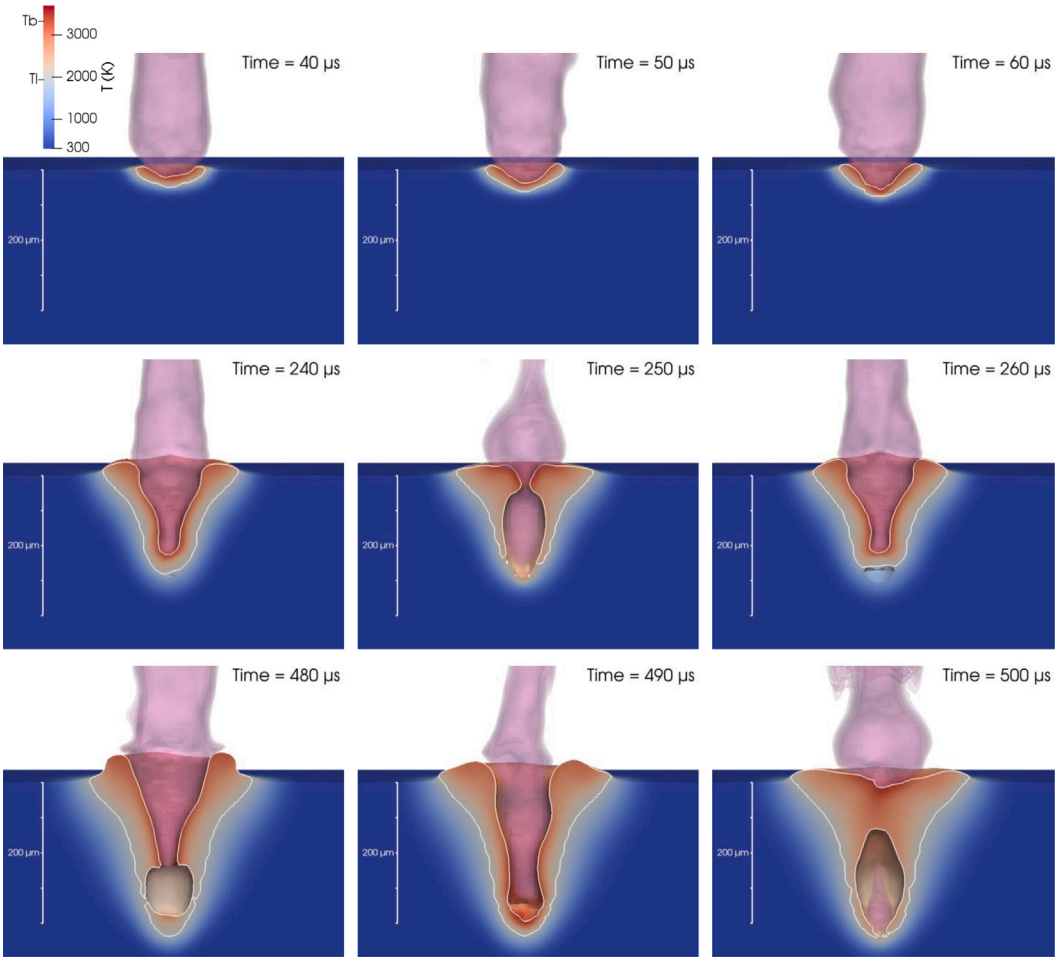

Fig. 13. Stationary Illumination of Ti6Al4V bare plate: P_{Laser} = 156 W, d_{Laser} = 95 µm. Temporal evolution of keyhole at three different stages, showing keyhole growth and collapse. Cut through domain half, showing condensed matter colored by temperature, and contour surfaces of metal vapor (purple) at different α_{vap}-iso-values within $0.5 < \alpha_{vap} < 1$, white line denotes $\alpha_{liquid} = 0.5$.

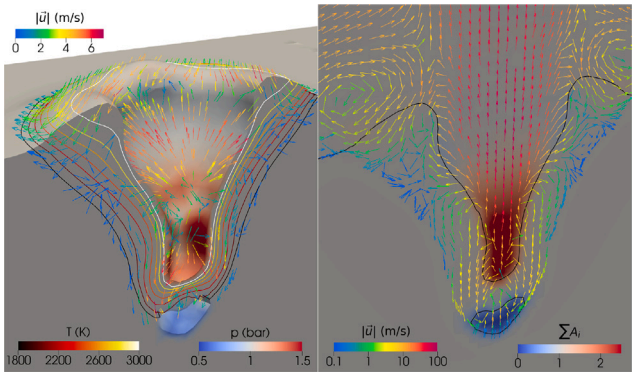

Fig. 14. Stationary Illumination of Ti6Al4V bare plate: P_{Laser} = 156 W, d_{Laser} = 95 µm. Result at t = 260 µs, cut through domain half, showing condensed matter colored by pressure with velocity vectors in liquid and temperature contour lines (left) and entire domain colored by $\sum A_i$, showing velocity vectors in liquid and gaseous phases (right).

Appendix. Material properties

The material properties of Ti6Al4V, Cu-ETP and ambient gas, used in the simulations presented in Sections 4.4 and 4.5 are provided here in detail. State-independent properties of Ti6Al4V, and properties of the material's solid, liquid and vapor state are listed in Tables A.4–A.7, respectively. State-independent properties of Cu-ETP, and properties of the material's solid, liquid and vapor state are listed in Tables A.8–A.11, respectively. The properties of ambient gas are provided in Table A.12. Temperature-dependent properties are linearly interpolated between the data points listed in the respective Tables.

The surface energy values of solid Ti6Al4V are chosen so that neither hydrophobic nor hydrophilic behavior is present, but approaching hydrophilic (wetting) conditions between solid and liquid at the melting point. The surface energy values of solid Cu-ETP are chosen so that hydrophobic behavior is present, as observed in the corresponding experiment of [58], but approaching the value of the liquid at the melting point, as there is no discontinuity across the melting point of Cu, as reported by [60]. The surface energy values of liquid Cu-ETP have been slightly reduced from those for pure Cu to account for the oxygen content of Cu-ETP [61].

Calculation of the viscosity using the kinetic theory is done following the approach of [62] via $\nu(T) = \nu_0(\rho_0/\rho)(T/T_0)^{0.5}$. Calculation of the viscosity using the ideal gas law follows the approach of [63].

The thermal conductivity values of metal vapor have been extrapolated from ambient gas values, as no data was available in literature, and the influence on the results is small. Values for the complex refractive index of solid Ti6Al4V were calculated to reproduce the experimentally observed bare plate absorptivity reported by [64]. As no values for the complex refractive index of liquid Cu-ETP was available in literature, the values were fitted to reproduce the experimentally obtained penetration depth reported by [58].

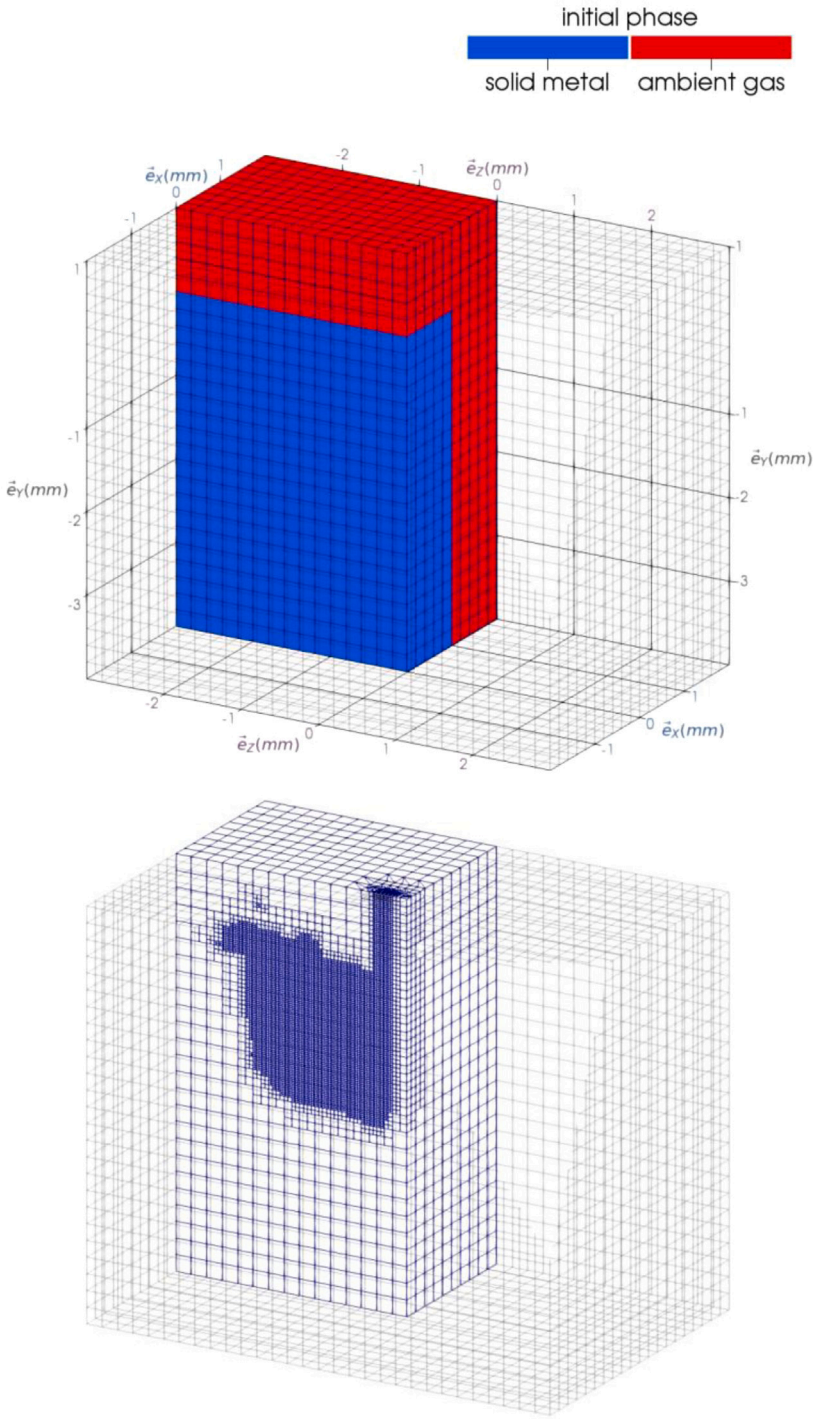

Fig. 15. Keyhole welding of copper: Computational domain, showing initial mesh and initial phase distribution (top), as well as dynamically refined mesh during simulation (bottom). To show the mesh refinement, the domain is cut in this image along the $\vec{e}_x$- and $\vec{e}_z$-direction, showing only a quarter of the initialized fields.

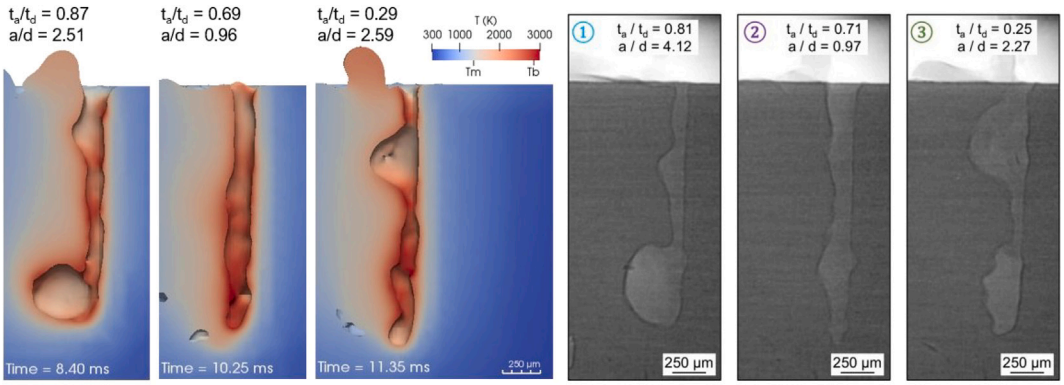

Fig. 16. Keyhole welding of copper: Comparison of maximum bulging positions observed in simulation (left) and experiment by Schricker et al. [58] (right).

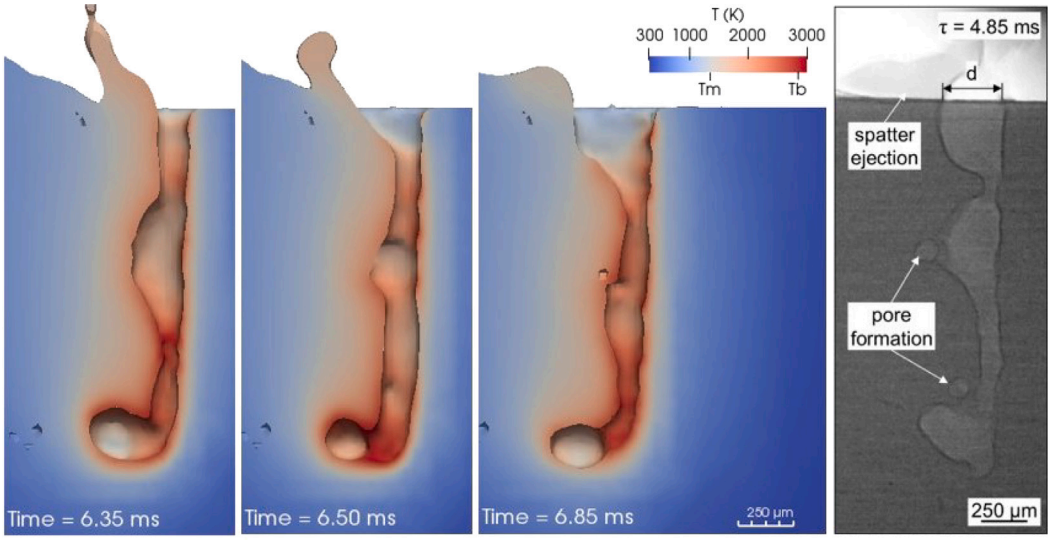

Fig. 17. Keyhole welding of copper: Comparison of spatter ejection and associated keyhole aperture increase, as well as pore formation due to pinch-off of upper bulge observed in simulation (left) and experiment by Schricker et al. [58] (right).

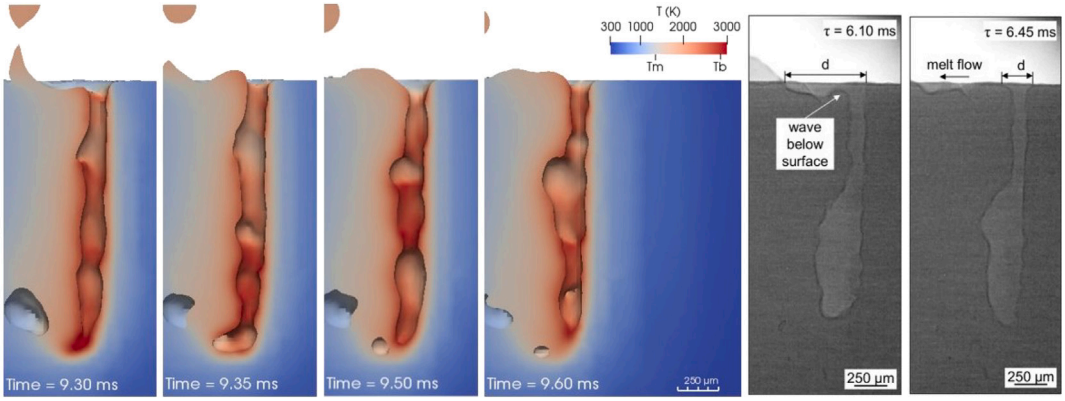

Fig. 18. Keyhole welding of copper: Comparison of backwards traveling surface wave following a large spatter event observed in simulation (left) and experiment by Schricker et al. [58] (right).

Table A.4
Material properties of Ti6Al4V: State-independent properties.

Property	T (K)	Value	Unit	Ref.
Ti6Al4V (general)				
Molar mass M	–	$46.77 \cdot 10^{-3}$	kg mol^{-1}	[65]
Solidus temperature $T_{solidus}$	–	1878	K	[65]
Liquidus temperature $T_{liquidus}$	–	1928	K	[65]
Boiling temperature $T_{boiling}$	–	3315	K	[65]
Latent heat (fusion) L_{fusion}	–	$2.9 \cdot 10^{5}$	m^2 s^{-2}	[65]
Latent heat (vaporization) L_{vap}	–	$9.82 \cdot 10^{6}$	m^2 s^{-2}	[65]

Table A.5
Material properties of Ti6Al4V: Solid state.

Property	T (K)	Value	Unit	Ref.
Ti6Al4V (solid)				
Density ρ	293	4457	kg m^{-3}	[65]
	973	4350	kg m^{-3}	[66]
	1873	4150	kg m^{-3}	[66]
Bulk modulus K	293	$119.2 \cdot 10^{9}$	kg s^{-2} m^{-1}	[67]
	773	$90 \cdot 10^{9}$	kg s^{-2} m^{-1}	[67]
	1928	$40 \cdot 10^{9}$	kg s^{-2} m^{-1}	[68]
Specific heat capacity c_p	293	580	m^2 s^{-2} K^{-1}	[67]
	873	668	m^2 s^{-2} K^{-1}	[69]
	1073	691	m^2 s^{-2} K^{-1}	[69]
	1278	643	m^2 s^{-2} K^{-1}	[69]
	1373	660	m^2 s^{-2} K^{-1}	[69]
	1923	759	m^2 s^{-2} K^{-1}	[69]
Thermal conductivity λ	430	5.957	kg m s^{-3} K^{-1}	[70]
	1270	17	kg m s^{-3} K^{-1}	[70]
	1383	19.87	kg m s^{-3} K^{-1}	[70]
	1888	27	kg m s^{-3} K^{-1}	[70]
Surface energy σ	300	0.375	kg s^{-2}	
	1500	1.0	kg s^{-2}	
	1878	1.505	kg s^{-2}	[71]
Refractive index n	–	3.86	–	[64]
Extinction coefficient κ	–	6.1	–	[64]

Table A.6
Material properties of Ti6Al4V: Liquid state.

Property	T (K)	Value	Unit	Ref.
Ti6Al4V (liquid)				
Density ρ	1923	4100	kg m^{-3}	[66]
	2073	4025	kg m^{-3}	[66]
	2573	3800	kg m^{-3}	[66]
Bulk modulus K	1928	$40 \cdot 10^{9}$	kg s^{-2} m^{-1}	[68]
	3315	$1 \cdot 10^{9}$	kg s^{-2} m^{-1}	
Kinematic viscosity ν	1732	$3.9 \cdot 10^{-6}$	m^2 s^{-1}	[71]
	1931	$2.53 \cdot 10^{-6}$	m^2 s^{-1}	[71]
	2045	$2.14 \cdot 10^{-6}$	m^2 s^{-1}	[71]
Surface energy σ	1928	1.505	kg s^{-2}	[71]
	3315	1.1	kg s^{-2}	[71]
Specific heat capacity c_p	–	1126	m^2 s^{-1} K^{-2} K^{-1}	[70]
Thermal conductivity λ	1913	28.8	kg m s^{-3} K^{-1}	[70]
	2666	42.2	kg m s^{-3} K^{-1}	[70]
Refractive index n	1901	4.01	–	[65]
	2603	4.08	–	[65]
Extinction coefficient κ	1901	4.7	–	[65]
	2603	4.83	–	[65]

Table A.7
Material properties of Ti6Al4V: Vapor state.

Property	T (K)	Value	Unit	Ref.
Ti6Al4V (vapor)				
Density ρ	–	*ideal gas law*		
Bulk modulus K	–	$1 \cdot 10^{5}$	kg s^{-2} m^{-1}	
Surface energy σ	–	0	kg s^{-2}	
Specific heat capacity c_p	3631	732	m^2 s^{-2} K^{-1}	[72]
	4000	774	m^2 s^{-2} K^{-1}	[72]
	4800	853	m^2 s^{-2} K^{-1}	[72]
Thermal conductivity λ	3315	0.1281	kg m s^{-3} K^{-1}	
	5000	0.1588	kg m s^{-3} K^{-1}	
Kinematic viscosity ν	–	*ideal gas law*		
Refractive index n	–	1	–	
Extinction coefficient κ	–	0	–	

Table A.8
Material properties of Cu-ETP: State-independent properties.

Property	T (K)	Value	Unit	Ref.
Cu-ETP (general)				
Molar mass M	–	$63.546 \cdot 10^{-3}$	kg mol^{-1}	[73]
Solidus temperature $T_{solidus}$	–	1347	K	[74]
Liquidus temperature $T_{liquidus}$	–	1347	K	[74]
Boiling temperature $T_{boiling}$	–	2854	K	
Latent heat (fusion) L_{fusion}	–	$2.056 \cdot 10^{5}$	m^2 s^{-2}	
Latent heat (vaporization) L_{vap}	–	$4.75 \cdot 10^{6}$	m^2 s^{-2}	

Table A.9
Material properties of Cu-ETP: Solid state.

Property	T (K)	Value	Unit	Ref.
Cu-ETP (solid)				
Density ρ	1347	8320	kg m^{-3}	[74]
Bulk modulus K	300	$100 \cdot 10^{9}$	kg s^{-2} m^{-1}	
Specific heat capacity c_p	300	385	m^2 s^{-2} K^{-1}	[72]
	973	440	m^2 s^{-2} K^{-1}	[72]
Thermal conductivity λ	273	390	kg m s^{-3} K^{-1}	[74]
	973	300	kg m s^{-3} K^{-1}	[74]
	1347	250	kg m s^{-3} K^{-1}	
Surface energy σ	300	0.1	kg s^{-2}	
	1339	0.1	kg s^{-2}	
	1340	1.135	kg s^{-2}	[61]
Refractive index n	–	0.35	–	[75]
Extinction coefficient κ	–	7.0	–	[75]

Table A.10
Material properties of Cu-ETP: Liquid state.

Property	T (K)	Value	Unit	Ref.
Cu-ETP (liquid)				
Density ρ	1350	7970.8	kg m^{-3}	[76]
	1700	7724.1	kg m^{-3}	[76]
Bulk modulus K	–	$1 \cdot 10^{9}$	kg s^{-2} m^{-1}	
Kinematic viscosity ν	1356	$5.04 \cdot 10^{-7}$	m^2 s^{-1}	[77]
	1500	$4.07 \cdot 10^{-7}$	m^2 s^{-1}	[77]
	1700	$3.24 \cdot 10^{-7}$	m^2 s^{-1}	[77]
	1950	$2.61 \cdot 10^{-7}$	m^2 s^{-1}	[77]
Surface energy σ	1347	1.135	kg s^{-2}	[61]
	2868	0.898	kg s^{-2}	[61]
Specific heat capacity c_p	–	516.86	m^2 s^{-1} K^{-2} K^{-1}	[72]
Thermal conductivity λ	1347	142	kg m s^{-3} K^{-1}	[78]
	2854	185	kg m s^{-3} K^{-1}	[78]
Refractive index n	–	0.96	–	
Extinction coefficient κ	–	6.2	–	

Table A.11
Material properties of Cu-ETP: Vapor state.

Property	T (K)	Value	Unit	Ref.
Cu-ETP (vapor)				
Density ρ	–	*ideal gas law*		
Bulk modulus K	–	$1 \cdot 10^5$	kg s^{-2} m^{-1}	
Surface energy σ	–	0	kg s^{-2}	
Specific heat capacity c_p	2900	387.9	m^2 s^{-2} K^{-1}	[72]
	3500	435.7	m^2 s^{-2} K^{-1}	[72]
	4500	498.2	m^2 s^{-2} K^{-1}	[72]
Thermal conductivity λ	3000	0.15	kg m s^{-3} K^{-1}	
	5000	0.24	kg m s^{-3} K^{-1}	
kinematic viscosity ν	–	*ideal gas law*		
Refractive index n	–	1	–	
Extinction coefficient κ	–	0	–	

Table A.12
Material properties of ambient gas.

Property	T (K)	Value	Unit	Ref.
Ambient gas				
Molar mass M	–	$28.014 \cdot 10^{-3}$	kg mol^{-1}	
Density ρ	–	*ideal gas law*		
Bulk modulus K	–	$1 \cdot 10^5$	kg s^{-2} m^{-1}	
Surface energy σ	–	0	kg s^{-2}	
Specific heat capacity c_p	300	1041.3	m^2 s^{-2} K^{-1}	[72]
	1800	1270.8	m^2 s^{-2} K^{-1}	[72]
Thermal conductivity λ	300	$2.597 \cdot 10^{-2}$	kg m s^{-3} K^{-1}	[72]
	900	$6.052 \cdot 10^{-2}$	kg m s^{-3} K^{-1}	[72]
	1800	$10.088 \cdot 10^{-2}$	kg m s^{-3} K^{-1}	[72]
Kinematic viscosity ν	–	*kinetic theory*		
		ν_0=$1.593 \cdot 10^{-5}$	m^2 s^{-1}	[72]
		ρ_0=1.1233	kg m^{-3}	[72]
		T_0=300	K	
Refractive index n	–	1	–	
Extinction coefficient κ	–	0	–	

References

[1] Steen W. Laser material processing—an overview. J Opt Pure Appl Opt 2003;5(4). http://dx.doi.org/10.1088/1464-4258/5/4/351.

[2] Shin YC, Wu B, Lei S, Cheng GJ, Lawrence Yao Y. Overview of laser applications in manufacturing and materials processing in recent years. J Manuf Sci Eng 2020;142(11):110818. http://dx.doi.org/10.1115/1.4048397.

[3] Otto A, Koch H, Leitz K-H, Schmidt M. Numerical simulations-a versatile approach for better understanding dynamics in laser material processing. Physics Procedia 2011;12:11–20. http://dx.doi.org/10.1016/j.phpro.2011.03.003.

[4] Zhao J, Cheng P. A lattice Boltzmann method for simulating laser cutting of thin metal plates. Int J Heat Mass Transfer 2017;110:94–103. http://dx.doi.org/10.1016/j.ijheatmasstransfer.2017.02.091.

[5] Cho J-H, Na S-J. Implementation of real-time multiple reflection and fresnel absorption of laser beam in keyhole. J Phys D: Appl Phys 2006;39(24):5372. http://dx.doi.org/10.1088/0022-3727/39/24/039.

[6] Courtois M, Carin M, Le Masson P, Gaied S, Balabane M. A new approach to compute multi-reflections of laser beam in a keyhole for heat transfer and fluid flow modelling in laser welding. J Phys D: Appl Phys 2013;46(50):505305. http://dx.doi.org/10.1088/0022-3727/46/50/505305.

[7] Tan W, Shin YC. Analysis of multi-phase interaction and its effects on keyhole dynamics with a multi-physics numerical model. J Phys D: Appl Phys 2014;47(34):345501. http://dx.doi.org/10.1088/0022-3727/47/34/345501.

[8] Ai Y, Jiang P, Shao X, Li P, Wang C. A three-dimensional numerical simulation model for weld characteristics analysis in fiber laser keyhole welding. Int J Heat Mass Transfer 2017;108:614–26. http://dx.doi.org/10.1016/j.ijheatmasstransfer.2016.12.034.

[9] Ai Y, Jiang P, Shao X, Li P, Wang C, Mi G, Geng S, Liu Y, Liu W. The prediction of the whole weld in fiber laser keyhole welding based on numerical simulation. Appl Therm Eng 2017;113:980–93. http://dx.doi.org/10.1016/j.applthermaleng.2016.11.050.

[10] Yu T, Zhao J. Quantitative simulation of selective laser melting of metals enabled by new high-fidelity multiphase, multiphysics computational tool. Comput Methods Appl Mech Engrg 2022;399:115422. http://dx.doi.org/10.1016/j.cma.2022.115422.

[11] Wu D, Hua X, Huang L, Zhao J. Numerical simulation of spatter formation during fiber laser welding of 5083 aluminum alloy at full penetration condition. Opt Laser Technol 2018;100:157–64. http://dx.doi.org/10.1016/j.optlastec.2017.10.010.

[12] Wang L, Zhang Y, Yan W. Evaporation model for keyhole dynamics during additive manufacturing of metal. Phys Rev A 2020;14(6):064039. http://dx.doi.org/10.1103/PhysRevApplied.14.064039.

[13] Cook PS, Ritchie DJ. Determining the laser absorptivity of Ti-6Al-4V during laser powder bed fusion by calibrated melt pool simulation. Opt Laser Technol 2023;162:109247. http://dx.doi.org/10.1016/j.optlastec.2023.109247.

[14] Feng Y, Gao X, Zhang Y, Peng C, Gui X, Sun Y, Xiao X. Simulation and experiment for dynamics of laser welding keyhole and molten pool at different penetration status. Int J Adv Manuf Technol 2021;112:2301–12. http://dx.doi.org/10.1007/s00170-020-06489-y.

[15] Flint TF, Scotti L, Basoalto HC, Smith MC. A thermal fluid dynamics framework applied to multi-component substrates experiencing fusion and vaporisation state transitions. Commun Phys 2020;3(1):196. http://dx.doi.org/10.1038/s42005-020-00462-7.

[16] Flint TF, Robson JD, Parivendhan G, Cardiff P. Laserbeamfoam: Laser ray-tracing and thermally induced state transition simulation toolkit. SoftwareX 2023;21:101299. http://dx.doi.org/10.1016/j.softx.2022.101299.

[17] Dal M, Fabbro R. An overview of the state of art in laser welding simulation. Opt Laser Technol 2016;78:2–14. http://dx.doi.org/10.1016/j.optlastec.2015.09.015.

[18] Cook PS, Murphy AB. Simulation of melt pool behaviour during additive manufacturing: Underlying physics and progress. Addit Manuf 2020;31:100909. http://dx.doi.org/10.1016/j.addma.2019.100909.

[19] Shu Y, Galles D, Tertuliano OA, McWilliams BA, Yang N, Cai W, Lew AJ. A critical look at the prediction of the temperature field around a laser-induced melt pool on metallic substrates. Sci Rep 2021;11(1):12224. http://dx.doi.org/10.1038/s41598-021-91039-z.

[20] Otto A, Koch H, Gómez Vázquez R. Multiphysical simulation of laser material processing. Physics Procedia 2012;39:843–52. http://dx.doi.org/10.1016/j.phpro.2012.10.109.

[21] Gómez Vázquez R, Koch H, Otto A. Multi-physical simulation of laser welding. Physics Procedia 2014;56:1334–42. http://dx.doi.org/10.1016/j.phpro.2014.08.059.

[22] Otto A, Patschger A, Seiler M. Numerical and experimental investigations of humping phenomena in laser micro welding. Physics Procedia 2016;83:1415–23. http://dx.doi.org/10.1016/j.phpro.2016.09.004.

[23] Otto A, Gómez Vázquez R. Fluid dynamical simulation of high speed micro welding. J Laser Appl 2018;30:032411. http://dx.doi.org/10.2351/1.5040652.

[24] Otto A, Gómez Vázquez R, Hartel U, Mosbah S. Numerical analysis of process dynamics in laser welding of Al and Cu. Procedia CIRP 2018;74:691–5. http://dx.doi.org/10.1016/j.procir.2018.08.040.

[25] Drobniak P, Otto A, Gómez Vázquez R, Arias RM, Arias JL. Simulation of keyhole laser welding of stainless steel plates with a gap. Procedia CIRP 2020;94:731–6. http://dx.doi.org/10.1016/j.procir.2020.09.134.

[26] Buttazzoni M, Zenz C, Otto A, Gómez Vázquez R, Liedl G, Arias JL. A numerical investigation of laser beam welding of stainless steelsheets with a gap. Appl Sci 2021;11:2549. http://dx.doi.org/10.3390/app11062549.

[27] Zenz C, Buttazzoni M, Martínez Ceniceros M, Gómez Vázquez R, Blasco Puchades JR, Portolés Griñán L, Otto A. Simulation-based process optimization of laser-based powder bed fusion by means of beam shaping. Addit Manuf 2023;77:103793. http://dx.doi.org/10.1016/j.addma.2023.103793.

[28] Otto A, Koch H, Gómez Vázquez R, Lin Z, Hainsey B. Multiphysical simulation of ns-laser ablation of multi-material LED-structures. Physics Procedia 2014;56:1315–24. http://dx.doi.org/10.1016/j.phpro.2014.08.057.

[29] Tatra S, Gómez Vázquez R, Stiglbrunner C, Otto A. Numerical simulation of laser ablation with short and ultra-short pulses for metals and semiconductors. Physics Procedia 2016;83:1339–46. http://dx.doi.org/10.1016/j.phpro.2016.08.141.

[30] Matsumoto H, Lin Z, Schrauben JN, Kleinert J, Gómez Vázquez R, Buttazzoni M, Otto A. Rapid formation of high aspect ratio through holes in thin glass substrates using an engineered, QCW laser approach. Appl Phys A 2022;128(4):1–10. http://dx.doi.org/10.1007/s00339-022-05404-4.

[31] Whitaker S. Flow in porous media I: A theoretical derivation of Darcy's law. Transp Porous Media 1986;1:3–25. http://dx.doi.org/10.1007/BF01036523.

[32] Rösler F, Brüggemann D. Shell-and-tube type latent heat thermal energy storage: numerical analysis and comparison with experiments. Heat Mass Transfer 2011;47(8):1027–33. http://dx.doi.org/10.1007/s00231-011-0866-9.

[33] Ruths M. Surface forces, surface tension, and adhesion. In: Wang QJ, Chung Y-W, editors. Encyclopedia of tribology. Boston, MA: Springer US; 2013, p. 3435–43. http://dx.doi.org/10.1007/978-0-387-92897-5_463.

[34] Brackbill JU, Kothe DB, Zemach C. A continuum method for modeling surface tension. J Comput Phys 1992;100(2):335–54. http://dx.doi.org/10.1016/0021-9991(92)90240-Y.

[35] Hirt CW, Nichols BD. Volume of fluid (VOF) method for the dynamics of free boundaries. J Comput Phys 1981;39(1):201–25. http://dx.doi.org/10.1016/0021-9991(81)90145-5.

[36] Koch M, Lechner C, Reuter F, Köhler K, Mettin R, Lauterborn W. Numerical modeling of laser generated cavitation bubbles with the finite volume and volume of fluid method, using openfoam. Comput & Fluids 2016;126:71–90. http://dx.doi.org/10.1016/j.compfluid.2015.11.008.

[37] Stein A. Simulation rotordynamischer problemstellungen mit der smoothed particle hydrodynamics methode. kassel university press GmbH; 2016.

[38] Voller VR, Prakash C. A fixed grid numerical modelling methodology for convection-diffusion mushy region phase-change problems. Int J Heat Mass Transfer 1987;30(8):1709–19. http://dx.doi.org/10.1016/0017-9310(87)90317-6.
[39] Dantzig JA, Rappaz M. Solidification: -Revised & expanded. EPFL Press; 2016.
[40] Watson KM. Thermodynamics of the liquid state. Ind Eng Chem 1943;35(4):398–406. http://dx.doi.org/10.1021/ie50400a004.
[41] Hügel H, Graf T. Laser in der fertigung. 2nd ed.. Springer; 2009.
[42] Beyer E. Schweißen mit laser. Berlin/Heidelberg, Germany: Springer; 1995.
[43] Jasak H. Error analysis and estimation for the finite volume method with applications to fluid flows (Ph.D. thesis), Imperial College London; 1996.
[44] Weller HG, Tabor G, Jasak H, Fureby C. A tensorial approach to computational continuum mechanics using object-oriented techniques. Comput Phys 1998;12(6):620–31. http://dx.doi.org/10.1063/1.168744.
[45] Rusche H. Computational fluid dynamics of dispersed two-phase flows at high phase fractions (Ph.D. thesis), Imperial College London; 2003, URL http://hdl.handle.net/10044/1/8110.
[46] Greenshields C, Weller H. Notes on computational fluid dynamics: General principles. Reading, UK: CFD Direct Ltd; 2022.
[47] The openfoam foundation: Openfoam 6 source code. 2022, URL https://github.com/OpenFOAM/OpenFOAM-6. accessed: 11.07.2022.
[48] Dritselis C, Karapetsas G. Open-source finite volume solvers for multiphase (n-phase) flows involving either Newtonian or non-Newtonian complex fluids. Comput & Fluids 2022;245:105590. http://dx.doi.org/10.1016/j.compfluid.2022.105590.
[49] Deshpande SS, Anumolu L, Trujillo MF. Evaluating the performance of the two-phase flow solver interfoam. Comput Sci Discov 2012;5(1):014016. http://dx.doi.org/10.1088/1749-4699/5/1/014016.
[50] Miller ST, Jasak H, Boger DA, Paterson EG, Nedungadi A. A pressure-based, compressible, two-phase flow finite volume method for underwater explosions. Comput & Fluids 2013;87:132–43. http://dx.doi.org/10.1016/j.compfluid.2013.04.002, USNCCM Moving Boundaries.
[51] Sod GA. A survey of several finite difference methods for systems of nonlinear hyperbolic conservation laws. J Comput Phys 1978;27(1):1–31. http://dx.doi.org/10.1016/0021-9991(78)90023-2.
[52] Greenshields CJ, Weller HG, Gasparini L, Reese JM. Implementation of semi-discrete, non-staggered central schemes in a colocated, polyhedral, finite volume framework, for high-speed viscous flows. Int J Numer Methods Fluids 2010;63(1):1–21. http://dx.doi.org/10.1002/fld.2069.
[53] Quintero F, Penide J, Riveiro A, Del Val J, Comesaña R, Lusquiños F, Pou J. Continuous fiberizing by laser melting (Cofiblas): Production of highly flexible glass nanofibers with effectively unlimited length. Sci Adv 2020;6(6):eaax7210. http://dx.doi.org/10.1126/sciadv.aax7210.
[54] Riveiro A, Quintero F, Boutinguiza M, Del Val J, Comesaña R, Lusquiños F, Pou J. Laser cutting: A review on the influence of assist gas. Materials 2019;12(1):157. http://dx.doi.org/10.3390/ma12010157.
[55] Quintero F, Doval AF, Goitia A, Gómez Vázquez R, Crespo K, Barciela R, Fernández-Arias M, Lusquiños F, Otto A, Pou J. Analysis of the oscillations induced by a supersonic jet applied to produce nanofibers. Int J Mech Sci 2023;238:107826. http://dx.doi.org/10.1016/j.ijmecsci.2022.107826.
[56] Cunningham R, Zhao C, Parab N, Kantzos C, Pauza J, Fezzaa K, Sun T, Rollett AD. Keyhole threshold and morphology in laser melting revealed by ultrahigh-speed x-ray imaging. Science 2019;363(6429):849–52. http://dx.doi.org/10.1126/science.aav4687.
[57] Kaplan AF. Analysis and modeling of a high-power yb: fiber laser beam profile. Opt Eng 2011;50(5):054201. http://dx.doi.org/10.1117/1.3580660.
[58] Schricker K, Schmidt L, Friedmann H, Diegel C, Seibold M, Hellwig P, Fröhlich F, Bergmann JP, Nagel F, Kallage P, Rack A, Requardt H, Chen Y. Characterization of keyhole dynamics in laser welding of copper by means of high-speed synchrotron X-ray imaging. Procedia CIRP 2022;111:501–6. http://dx.doi.org/10.1016/j.procir.2022.08.079.
[59] Roenby J, Bredmose H, Jasak H. A computational method for sharp interface advection. R Soc Open Sci 2016;3(11):160405. http://dx.doi.org/10.1098/rsos.160405.
[60] Udin H. Surface tension of solid copper (Ph.D. thesis), Massachusetts Institute of Technology; 1949.
[61] Harrison DA, Yan D, Blairs S. The surface tension of liquid copper. J Chem Thermodyn 1977;9(12):1111–9. http://dx.doi.org/10.1016/0021-9614(77)90112-4.
[62] Bauman PT, Kirk BS, Oliver TA, Plessis S, Stogner RH. Antioch: C++ chemical kinetics, thermodynamics, and transport library. 2023, URL https://github.com/libantioch/antioch. accessed: 05.05.2023.
[63] Bird RB, Stewart WE, Lightfoot EN. Transport phenomena. Wiley & Sons; 2007.
[64] Simonds BJ, Tanner J, Artusio-Glimpse A, Williams PA, Parab N, Zhao C, Sun T. The causal relationship between melt pool geometry and energy absorption measured in real time during laser-based manufacturing. Appl Mater Today 2021;23:101049. http://dx.doi.org/10.1016/j.apmt.2021.101049.
[65] Yang Z, Bauereiß A, Markl M, Körner C. Modeling laser beam absorption of metal alloys at high temperatures for selective laser melting. Adv Energy Mater 2021;23(9):2100137. http://dx.doi.org/10.1002/adem.202100137.
[66] Schmon A, Aziz K, Pottlacher G. Density of liquid Ti-6Al-4V. EPJ Web Conf 2017;151:04003. http://dx.doi.org/10.1051/epjconf/201715104003.
[67] Welsch G, Boyer R, Collings EW. Materials properties handbook: Titanium alloys. ASM International; 1993.
[68] Starodubtsev YN, Tsepelev VS. Effect of atomic size on the isothermal bulk modulus and surface tension of liquid metals. Metall Mater Trans B 2022;53(4):2547–52. http://dx.doi.org/10.1007/s11663-022-02550-1.
[69] Zhao X, Reilly C, Yao L, Maijer DM, Cockcroft SL, Zhu J. A three-dimensional steady state thermal fluid model of jumbo ingot casting during electron beam re-melting of Ti–6Al–4V. Appl Math Model 2014;38(14):3607–23. http://dx.doi.org/10.1016/j.apm.2013.11.063.
[70] Boivineau M, Cagran C, Doytier D, Eyraud V, Nadal MH, Wilthan B, Pottlacher G. Thermophysical properties of solid and liquid Ti-6Al-4V (TA6V) alloy. Int J Thermophys 2006;27:507–29. http://dx.doi.org/10.1007/PL00021868.
[71] Wunderlich RK. Surface tension and viscosity of industrial ti-alloys measured by the oscillating drop method on board parabolic flights. High Temp Mater Process 2008;27(6):401–12. http://dx.doi.org/10.1515/HTMP.2008.27.6.401.
[72] Lemmon EW, Bell IH, Huber ML, McLinden MO. Thermophysical properties of fluid systems. In: Linstrom P, Mallard W, editors. NIST chemistry webbook, NIST standard reference database 69. National Institute of Standards and Technology, http://dx.doi.org/10.18434/T4D303.
[73] Wieser ME. Atomic weights of the elements 2005 (IUPAC technical report). Pure Appl Chem 2006;78(11):2051–66. http://dx.doi.org/10.1351/pac200678112051.
[74] Matweb Cu-ETP data sheet. 2023, URL https://www.matweb.com/. accessed: 12.05.2023.
[75] Johnson PB, Christy RW. Optical constants of the noble metals. Phys Rev B 1972;6(12):4370. http://dx.doi.org/10.1103/PhysRevB.6.4370.
[76] Kurochkin AR, Popel' PS, Yagodin DA, Borisenko AV, Okhapkin AV. Density of copper-aluminum alloys at temperatures up to 1400 C determined by the gamma-ray technique. High Temp 2013;51(2):197–205. http://dx.doi.org/10.1134/S0018151X13020120.
[77] Assael MJ, Kalyva AE, Antoniadis KD, Michael Banish R, Egry I, Wu J, Kaschnitz E, Wakeham WA. Reference data for the density and viscosity of liquid copper and liquid tin. J Phys Chem Ref Data 2010;39(3):033105. http://dx.doi.org/10.1063/1.3467496.
[78] Alter L, Heider A, Bergmann J-P. Investigations on copper welding using a frequency-doubled disk laser and high welding speeds. Procedia CIRP 2018;74:12–6. http://dx.doi.org/10.1016/j.procir.2018.08.003.